Shallow Thermal Conditions in the Central and Southern Cascadia Subduction Zone

J.R. McKenna[1] and D.D. Blackwell[1]

[1]Department of Geological Sciences
Southern Methodist University
Dallas, Texas
75275

jmckenna@post.smu.edu
blackwel@passion.isem.smu.edu

For submission to Journal of Geophysical Research, 3/20/02

ABSTRACT

We have investigated the influence of temperature along the very young (< 8 Ma), presently seismically quiescent central and southern Cascadia subduction zone (CSZ) to gain insight into hypothesized great ($M_w > 9$) subduction zone thrust earthquakes. Thermal cross-sections based on measured heat flow and the properties of the overlying accretionary complex and adjacent backstop are used to characterize the temperature of the shallow décollement (≤ 30 km) within these segments of the subduction zone. Eight new heat flow determinations (offshore) are used, in conjunction with existing heat flow data and a theoretical surface heat flow value at the deformation front, to establish a complete surface heat flow profile across the CSZ in northern Oregon (45 °N). A heat flow profile north of the Mendocino Triple Junction (MTJ) in northern California (40 °N), utilizing existing heat flow data and a theoretical deformation front heat flow value, was also constructed to investigate the thermal effects of subduction of the even younger Gorda plate and to compare the seismicity in the MTJ area with our thermal model for the CSZ. Thermal cross-sections were constructed using the following methodology. Heat generation was removed from a "low" and "high" surface heat flow profile to obtain a basal (i.e., along the décollement) heat flow boundary condition. Two-dimensional, finite difference calculations utilizing this boundary condition were used to model the CSZ forearc thermal regime. Strength envelopes and steady-state pressure-temperature paths calculated from temperature-depth data sampled along the subducting plate-top illustrate the low strength along the slab-face.

INTRODUCTION

Previous Studies and Regional Tectonics

In the Pacific Northwest region of the united States, subduction of young Juan de Fuca (JDF) lithosphere is occurring at approximately 45 mm/yr oriented 68º [e.g., *Demets et al.*, 1990] to the North American plate. The seismicity of the region is plotted by hypocentral depth on a tectonic map of the study area depth on Figure 1. The anomalous character of the Cascadia Subduction Zone (CSZ) is immediately obvious because, based on the instrumental record, almost no shallow thrust (interslab) earthquakes have occurred in the forearc region. Most regional seismicity is restricted to strike-slip events from the Mendocino and Blanco Transform Faults, intraslab events in the Puget Sound area of Washington State and coastal northern California, and shallow events in the Cascade volcanic arc [*Crosson and Rogers*, 1999]. However, there is significant evidence that a large shallow thrust fault earthquake occurred about 300 years ago along the CSZ [e.g., *Atwater*, 1987]. Hence, significant research efforts have been devoted to analysis of probable 9+ (M_w) shallow thrust events along the Cascadia margin in an area that has been seismically quiescent for at least 100 years. To compare Cascadia with seismically active subduction zones hazard analysis studies have utilized regional seismicity [*Heaton and Kanamori*, 1984; *Heaton and Hartzell*, 1987; *Rodgers*, 1988; *Ruff and Kanamori*, 1980; *Tichelaar and Ruff*, 1993], geodetic and structural constraints [*Savage et al.*, 1991; *Snay and Matsikari,* 1991; *Dragert et al.*, 1994, *Goldfinger et al.,* 1997; *McNeil et al.*, 2000], paleoseismic arguments [*Atwater*, 1987; *Satake and Tanioka*, 1999], and thermal modeling to constrain the seismogenic zone [*Blackwell and Eckhardt*, 1991; *Hyndman and Wang* 1993; *Hyndman and Wang,*, 1995]. Two review articles by *Atwater et al.* [1995] and *Nelson and Personius* [1996] discuss more extensively the evidence (past and present) for large thrust

(interplate) earthquakes along the Cascadia margin.

Detailed published thermal modeling utilizing the surface heat flow so far has been confined to the northern limits of the JDF plate [*Lewis et al*., 1988; *Hyndman and Wang*, 1993; *Hyndman and Wang*, 1995; *Wang et al*., 1995a], however, some attempts to characterize the general thermal structure of the entire margin have been described [*Blackwell and Eckhardt*, 1991; *Hyndman and* Wang, 1995; *Hyndman et al*, 1997; *Oleskevich et al*., 1999]. The onshore outer and volcanic arc heat flow within the middle-southern Cascadia forearc (i.e., mid-Oregon to northern California) has been described in detail and is arguably the best known of any active subduction zone and [*Blackwell et al.,* 1982; *Blackwell et al.*, 1990a; *Blackwell et al.*, 1990b]. However, the addition of two ODP heat flow measurements in the Oregon accretionary prism [*Westbrook, Carson, Musgrave, et al.*, 1994] that have helped to fill the data gap between the onshore Oregon data and the Cascadia Basin data presented by *Korgen et al.*, [1971] and *Moran and Lister*, [1987] there remains a data gap between the deformation front and the coast (about 100 km). With the exception of two recent ODP heat flow sites [*Lyle, Koizumi, Richter et al*., 1997] no data exist for offshore northern California, and only a few measurements are available onshore [*Lachenbruch and Sass*, 1980; *Mase et al*., 1982].

There are three objectives of this paper. The first is to present new heat flow data for the continental margin of Oregon. This new data, along with existing offshore and onshore data allow an almost complete heat flow cross section to be developed for the Cascadia subduction zone off of Oregon. The completeness of this section is unique for active subduction zones. The second objective of the paper is to develop a thermal model of the slip zone (plate interface) based on the recognition that the rocks of the outer arc block have very low permeability and heat transfer is entirely conductive, and to use this thermal model to examine the rheological

properties of the subduction zone. This predominantly conductive heat transfer allows a straightforward calculation of the temperature on the slip zone using the well-determined surface heat flow profile. This same technique is also applied to develop a thermal cross section at the south end of the Cascadia subduction zone in California just north of the Mendocino Triple Junction (MTJ). The California section has been included, not because a high quality thermal profile can be constructed there, but to use this simple approach to estimate the thermal conditions in a place where the subducting plate is very young and where there is interface seismicity associated with the subducting slab. Thus the integrated strength predictions obtained from strength envelope analysis can be tested in this setting. These two sections, together with published sections, allow a reasonably complete picture to be drawn of the Cascadia subduction zone from north to south [e.g., *Hyndman and Wang*, 1993]. The third objective of the paper is to place the thermal regime of the Cascadia subduction zone in a larger perspective by comparing the thermal regime to "classical" subduction zones that are associated with blueschist facies metamorphism. This is necessary because high quality complete thermal sections of presently active subduction zones are almost nonexistent. The comparison is made using a petrogenic grid and comparing and contrasting the metamorphic facies predicted in different subduction zones.

We also emphasize two points regarding our modeling procedure. First, the approach outlined in this study calculates the temperature along the slab interface based on an extrapolation of the surface heat flow field. This is essentially the downward continuation method [*Brott et al.*, 1981], and is based on the assumption that the modeled region is dominated by conduction. This approach is appropriate for the Cascadia forearc specifically, and almost all forearcs generally, because of both the low bulk permeability of both forearc volcanics and

sediments. *Blackwell et al.* [1982, 1990] have demonstrated that volcanics of basaltic and andesitic composition are essentially impermeable when thermally altered at low to moderate temperatures. Furthermore the shales and siltstones of the forearc are intrinsically low permeability units except along major faults. Also there is a lack of any unexplained thermal anomalies present between the deformation front and volcanic arc [*Blackwell et al.*, 1982], strongly suggesting that the entire Cascadia forearc is conductive. Second, because our models solve the conductive problem above the subducting slab and take the temperature on the interface as a boundary condition on the solution, the temperatures below this boundary in the moving slab are not relevant to the forearc thermal regime.

Satisfying the basal heat flow boundary condition in this manner accomplishes three things. One, it eliminates the need to specify the deep, unconstrained thermal structure of the subducting slab to obtain a solution. Two, by reducing the vertical scale of the model (i.e., by solving the problem above the décollement), it obviates the necessity of including any possible deep (mantle), convection. Three, this methodology automatically satisfies the observed surface profile. Thus, this approach demonstrates the power of using the surface heat flow to accurately constrain the thermal regime of the subduction interface in contrast to most models which focus on the less well known and less well constrained deep effects and thus have errors that are difficult to evaluate and constrain and may not generate realistic surface heat flow distributions.

NEW THERMAL DATA

Bottom-Hole Temperature Data

Investigation of the forearc thermal regime of the southern segment of the Cascadia subduction zone (CSZ) has been limited by a paucity of thermal data between the deformation front and coast (see the lower half of Figure 2). The first objective of this paper is to address

this data gap by describing eight new heat flow determinations along the Oregon continental shelf and coast utilizing bottom-hole temperature (BHT) data from hydrocarbon exploration wells. These new measurements help minimize the data-gap by providing additional constraints on the surface heat flow profile close to the deformation front, and thus, provide a boundary condition on thermal models of the CSZ.

In hydrocarbon exploration wells, a continuous record of temperature with depth is not usually available. Instead, a measurement of "maximum" temperature, presumed to be at the well bottom when logged, is recorded at various depths during geophysical logging runs as the well is drilled. The locations of the seven offshore and seven onshore exploration wells with available BHT data as listed in Table 1. All these wells were drilled in the 1960's in an effort to locate hydrocarbon accumulations. The wells used for heat flow determinations are shown by name in the upper part of Figure 2, whereas the wells that possessed BHT data only (i.e., no heat flow was determined from the BHT data) are simply plotted as well symbols. The unprocessed BHT data from each well are plotted as a function of depth in Figure 3a. Three very similar temperature measurements (within 3 °C of each other) recorded at a depth of 2745 m in well P-093 were averaged and used as the one BHT measurement at that depth. A BHT correction should be applied, because drilling alters the thermal regime of a well by adding heat near the top and carrying it away at depth [e.g., *Funnell* et al., 1996]. Many different corrections have been suggested for BHT data [e.g., *Harrison et al.*, 1983; *Lee et al.*, 1996; *Gallardo and Blackwell*, 1999; *Forster*, 2001]. *Blackwell and Richards* [unpublished data] compared BHT correction techniques using a set of wells with equilibrium temperature logs and BHT data. For wells with only single point temperatures (i.e. no repeated sequences of loggings at the same depth over a period of hours) a simple polynomial correction as a function of depth seemed to

work the best. Therefore a simple second-order polynomial fit to the expression determined by *Harrison et al.* [1983] was utilized to correct the dataset presented in this study: $\Delta°C = -1.510 \times 10^{1} + 1.755 \times 10^{-2} \cdot z - 2.288 \times 10^{-6} \cdot z^{2}$, where $\Delta°C$ is the difference between the measured BHT and the "true" equilibrium formation temperature, and z is depth measured in meters. Only BHT measurements from depths greater than 915 m were corrected; at shallower depths, drilling disturbances are too numerous and effects too contradictory to justify application of any one correction factor.

Corrected BHT data are plotted in Figure 3b. Most deep temperatures have been raised an average of 10-15 °C while the shallowest temperatures have remained unchanged. Assuming a mean annual surface temperature of 10 °C, least-squares analysis of the bottom hole temperature data set yields a corrected temperature gradient (± one standard deviation) of 27.9 ± 0.9 °C/km, a difference of about 5 °C/km from the uncorrected temperature gradient of 22.6 ± 0.9 °C/km. The temperature-depth data of this set of wells shows remarkable consistency for the combined data set of both onshore and offshore BHT data. Based on this data set there is no evidence of significant lateral variations in thermal gradient over the large area investigated by the wells. Apparently, very similar thermal conditions occur regionally in the sediment dominated accretionary complex and basaltic volcanic backstop (i.e., Cascadia forearc) [see *Blackwell and Steele*, 1992].

Heat Flow

Fourier's Law is used for one-dimensional, steady state, heat conduction calculations and is:

$$q_s = -k \, dT/dz, \qquad (1)$$

where q_s is the surface heat flux per unit area (mWm^{-2}), k is the thermal conductivity ($Wm^{-1}K^{-1}$),

and dT/dz is the thermal gradient (°C/km). The negative sign is a convention indicating that heat flows in the direction of decreasing T.

Equation (1) may be recast into a more suitable form in which variations in thermal conductivity, and therefore, lithology, may be introduced. The inverse of thermal conductivity is thermal resistance (m^2KW^{-1}). The thermal resistance of a number of stacked layers may be summed algebraically to give the total thermal resistance of the stack. So $\Sigma \Delta z_i / k_i$ is the total thermal resistance, and if ΔT is $T_z - T_s$, where T_z is the temperature at depth z and T_s is the surface temperature. Thus,

$$T_z = q_s R + T_s \qquad (2)$$

A plot of T_z vs. R is often called a Bullard plot [*Bullard*, 1946]. The slope on a Bullard plot is the heat flow, and the intercept is T_s.

The lithology of the wells used to generate the heat flow determinations has been described as a part of onshore-offshore stratigraphic correlation studies of the Washington and Oregon continental margin [*Snavely*, 1981; *Snavely et al.*, 1981]. There are three dominant rock types: basalt, sandstone, and fine-grained sedimentary rocks, predominantly claystones and siltstones. In determining the thermal conductivity of these rock types, claystones and siltstones in this region are grouped together and assigned a value of 1.37 $Wm^{-1}K^{-1}$, basalts are assigned a value of 1.57 $Wm^{-1}K^{-1}$, and sandstones (which make up a very minor component of sediments on this continental margin) a value of 2.5 $Wm^{-1}K^{-1}$. These values are based on numerous measurements described by *Blackwell et al.*, [1982; 1990a; 1990b], and are based on onshore equivalent lithologies. These thermal conductivity values are typical for the Cascadia margin. For example, *Hyndman and Wang* [1993] utilized a value of 2.0 $Wm^{-1}K^{-1}$ to represent the Crescent Terrane component in their thermal modeling of the Vancouver margin. The Crescent

basalts are equivalent to the Eocene basalts (i.e., Siltez Terrane) that compose the basement of offshore Oregon. Composite thermal conductivity data are summarized for each well in Table 2.

It is unusual for offshore wells to have a lithologic record for their first several hundred meters. These portions of the well are commonly unconsolidated, fine-grained sediments, and samples are usually not retained. A thermal conductivity value of 1.37 $Wm^{-1}K^{-1}$ was assumed for the sediments missing from this portion of the well so that a complete record of thermal conductivity values exists between surface temperature and deepest BHT measurement. When available, geophysical (sonic) well logs were used to "fine-tune" the lithologic sequence of each offshore well, especially in the identification of the many basaltic dikes present in well P-087 [*Snavely et al*., 1981].

Fortunately, most of the wells have BHT measurements recorded at several different depths, allowing a more accurate thermal gradient calculation when combined with thermal resistance data, and heat flow determination. Lithology information (and thus, thermal conductivity data) is only available for 8 of the 14 wells. Bullard plots using uncorrected BHT data for the 8 wells in which heat flow determinations were made are presented in Figure 4a. Figure 4b illustrates the effect that correcting the BHT data set for drilling disturbances has on the calculated heat flow. This correction "un-kinks" most of the curves, rotating individual line segments closer to parallelism, the net effect of which is to produce a more linear cumulative resistance (and thus, constant heat flow) profile for each well. So while the error for individual wells may be high, the self-consistency of the complete data set is encouraging evidence that the average heat flow and thermal gradient to at least 3 km depth is well determined and has only a small possible variation over this large area. The mean heat flow from each well is presented in

Table 2. A least squares fit to the entire data set (offshore and onshore) yielded an uncorrected heat flow of 31.9 ± 4.2 mWm^{-2}, and a corrected heat flow of 39.8 ± 5.1 mWm^{-2}.

From Figure 4b it is also apparent that heat flow is not the same for the onshore and offshore wells: the onshore wells have lower heat flow values of at least 4 mWm^{-2}, or about 10% lower. Below about 1500 m, the Bullard plots for the wells constitute two roughly parallel groups, the lower of which are the continental wells, GLB-1 and SFM-1. This result is not unexpected, as the onshore wells are located farther east (and farther downdip), and might therefore experience a reduced mantle heat flux as a result of the increasing age and depth of the subducting Juan de Fuca lithosphere.

Worldwide forearc heat flow values beginning a few kilometers from the deformation front values tend to cluster around 40 mWm^{-2} [e.g., *Clark et al*., 1978; *Lewis et al*., 1985; *Ziagos et al.*, 1985; *Matsubayashi et al*., 1992*; Ferguson et al*., 1993; *Langseth and Si*lver, 1996; *Springer and Forster*, 1998; *von Herzon et al*, 2001], similar to CSZ forearc heat flow measurements [lower part of Figure 2; also see *Blackwell et al.*, 1982; 1990a; 1990b]. The uniformity of these measurements globally as well as on the local scale suggests that, with few exceptions, the outer-arc of subduction zones, is wholly conductive, and therefore, well suited to the simple two-dimensional conductive modeling we present in this study. Figure 5 is a cartoon illustrating the appropriateness of this assumption. Regardless of local non-conductive processes at and near the slab face, the heat flux off the subducting oceanic crust is conductive throughout the forearc block. This conductive flux is denoted by the groups of arrows emanating from the solid black at the top of the subducting crust (i.e. thrust interface). In fact, the only area probably advectively disturbed by hydrothermal convection is enclosed by the crosshatched area in Figure 5, whereas the remaining accretionary complex material and proto-thrust area is

conductive (area indicated by dotted arrows). This disturbed area is usually at, or seaward of the deformation front, and is most likely limited to the permeable pathways in the upper 1 km of the sediment column [*Davis et al*, 1996]. Only rarely does this perturbation affect the actual décollement, in which case it causes hydrothermal cooling of the oceanic crust and disturbs the thermal regime sufficiently to mask the mantle heat flow, q_m (see *Langseth and Silver*, [1996]; *Silver*, [2001] for an illustration of this effect in the northern Costa Rica subduction zone). In fact, the linearity of the forearc temperature-depth curves (or equivalently, the Bullard plots in Figure 4) are consistent with low permeability rock types at depth, due to lithology and perhaps thermal alteration [*Davis et al*., 1996].

THERMAL CROSS-SECTIONS

Surface heat flow profiles

The second objective of this study is to investigate the thermal regime of the outer arc block of the CSZ in Oregon and Northern California. Heat flow data within 200 km to the north or south of 45 °N were projected onto that latitude to form the Oregon profile (Figure 6a). Similarly, heat flow data in northern California between 40-41°N were projected onto a profile at about 40.5°N (Figure 7a). However, because small latitudinal changes in the vicinity of the Mendocino Triple Junction can lead to large changes in heat flow, and because the strike of the structural cross-section is not exactly N-S, data points were projected orthogonally onto the profile, rather than simply collapsing the data (preserving longitude/latitude, compare Figures 2 and 7a). This procedure preserves the relationship between increasing age of the subducted plate, and exponentially decreasing surface heat flow.

Northern Oregon heat flow measurements west of and just east of the deformation front on the Juan de Fuca plate are scattered, varying from 40-150 mWm^{-2} [*Korgen et al.*, 1971;

Moran and Lister, 1987; *Westbrook et al*., 1994; *Davis et al.*, 1997; *McKenna*, 1997]. The average heat flow is generally high and is similar to that expected from a crust of appropriate age because of the thick blanket of relatively impermeable sediment on top of the ocean crust even west of the deformation front (about 3 km thick, see Figure 6b). However, beginning at a distance of about 20 km east of the deformation front heat flow remains relatively constant at about 40 mWm^{-2}, until the Cascade Range volcanic arc thermal anomaly is reached (about 155 km east of the east end of the sections shown in Figures 6a and 7a).

Only two offshore heat flow measurements exist for northern California [*Lyle et al*., 1997]. Onshore heat flow west of the Cascade Range at this latitude is scattered, but averages 55 mWm^{-2}. This "elevated" forearc heat flow can be explained by the subduction of very young lithosphere in conjunction with significant heat generation within the Franciscan complex (discussed below).

A wide scatter occurs in the numerous measured heat flow data near the deformation front in northern Oregon (Figure 6a). Heat flows as low as 35 mWm^{-2}, but as high as 140 mWm^{-2} have been measured. Similarly, the only two heat flow measurements from offshore northern California are highly disparate. A heat flow measurement about 3 km seaward of the deformation front is only 57 mWm^{-2}, whereas a measurement 40 km farther west is 170 mWm^{-2} (Figure 7a). Thus the appropriate heat flow value at the deformation front (trench axis) is uncertain. The selection of this particular heat flow value is critical in the modeling. Underestimating this value results in lowering of the basal heat-input, depressing model isotherms locally. In contrast, overestimating the heat flow results in increasing the basal heat-input, raising isotherms at the deformation front.

In this study the heat flow profile for each cross section was anchored at the theoretical

heat flow corresponding to (insulated and cooling) oceanic lithosphere of the age of the plate at the deformation front [e.g., *Parsons and Sclater*, 1977]. To calculate temperatures the overlying sediment column thickness z, and heat generation, A, were taken into account using:

$$q_s = T_m\, k_m\, (\pi\kappa t)^{-1/2} + Az. \qquad (3)$$

The assumed boundary temperature of the lithosphere at the ridge (T_m), is 1350 °C; k_m, the thermal conductivity of the cooling slab is 2.5 $Wm^{-1}K^{-1}$; and κ, the thermal diffusivity, is 10^{-6} m^2/s [e.g., *Turcotte and Schubert*, 1982]. Generally the sediment column is not thick enough for the radiogenic heat production to contribute significantly to q_s. In the Cascadia forearc sediment heat generation is low, typically about 0.5 $\mu W/m^3$ [*Hyndman and Wang*, 1993; *McKenna*, 1997]. So even with a 3 km sediment layer at the deformation front, heat generation in the sediments overlaying the ocean crust in the northern Oregon forearc contributes only about 1.5 mWm^{-2} to the deformation front heat flow. Assuming the same heat generation for the forearc sediments at the deformation front in the northern California subduction zone, where sediment thickness is even thinner, results in less of a contribution. We therefore neglect this contribution to the deformation front surface heat flow as it is much less than the uncertainties involved in the calculation.

The surface heat flow obtained from equation (3) does not incorporate the effects of episodic fluid flow or other thermal disturbances. We feel that this approach has two advantages. First, the theoretical heat flow is the best estimate of the average steady-state heat flow experienced by the shallowest décollement. Second, the determination of the actual heat flow depends only on the age on the subducting oceanic crust at the deformation front. The heat flow obtained from equation (3) for the 8 Ma plate at the northern Oregon deformation front of 139 mWm^{-2} is bracketed by the observed data, which have a high scatter due to local

nonconductive processes (Figure 6a). The heat flow at the 5 Ma northern California deformation front predicted by equation (3) is 170 mWm^{-2} (Figure 7a). Unlike the northern Oregon data, the number of heat flow observations (i.e., 2) near the deformation front is not sufficient to determine the actual surface heat flow in northern California. However, because the nonconductive processes responsible for the heat flow scatter will affect the surface heat flow more than the basement temperature, the best estimate of the mean basement temperature may be represented by equation (3).

All surface heat flow data across the profiles are presented in Figures 6a and 7a for the northern Oregon and northern California profiles, respectively. The data include the theoretical deformation front heat flow derived from equation (3) (stars), ODP heat flow estimates (filled triangles), and the new Oregon continental margin heat flow developed in this study (well symbols) in addition to published heat flow measurements (filled squares). For both areas, an upper and lower heat flow curve is fit to the data (Figures 6a, and 7a). These curves are shown to quantify the trend of decreasing heat flow as the coast is approached. However, seaward of the deformation front the heat flow is poorly constrained, especially the northern California profile, resulting in an uncertain temperature distribution in the subducting slab just before it enters the trench. This uncertainty of the incoming slab thermal structure does not impact the calculated downdip décollement temperatures, as is discussed below. *Wang et al.* [1995a] have utilized the sediment compaction/fluid expulsion model of *Hutchison* [1985] to generate a one-dimensional temperature profile seaward of the deformation front to constrain the lithospheric thickness, and thus, basal lithospheric temperature boundary condition for subsequent finite-element modeling. Their approach yields a plate-top temperature of about ~260 °C for 6.5 Ma subducting crust. Simply inverting the theoretical heat flow value for the plate-top temperature

of a 5 Ma subducting crust (northern California) results in a temperature of about 227 °C (180 °C for the 8 Ma northern Oregon slab). Because the emphasis of the present study is not to generate a comprehensive thermal model of the actively folding sediments in the accretionary prism, but rather, investigate the effect of interface temperature on downdip décollement seismicity, we believe that the error introduced by using this simple formulation is acceptable.

Northern Oregon Thermal Models

To calculate temperatures and create thermal cross sections, the heat generation and thermal conductivity of the volcanics, claystones, and siltstones that comprise the accretionary wedge and continental backstop must be established. Sandstones appear in almost negligible quantities so their contribution to heat generation is not considered further. The average gamma-ray log counts for shale, siltstone and basalt units in the study wells derived from bore-hole gamma–ray logs obtained from several of the offshore wells are 49.5, 34.5, and 16.9 API counts, respectively. The standard gamma-ray well log unit used in the petroleum industry (API) is related to heat generation, A, by the empirical relationship [*Rybach*, 1985]:

$$A\ (\mu Wm^{-3}) = 0.0145[(API) - 5] \quad (4)$$

Equation (4) yields reasonable heat generation values of 0.17 μWm^{-3} for basalt, 0.43 μWm^{-3} for siltstones, and 0.65 μWm^{-3} for shales (Table 2). The latter two values are well constrained and are taken as the end-member heat generation values of sedimentary rocks within the subduction complex. There is evidence [*Snavely et al.*, 1981] that the basalts of wells P-087 and P-103 are similar to the Siletz volcanics that form the continental shelf and serve as a "subduction backstop". Rocks below the sediment cover in this region are therefore assigned a basaltic heat generation value. The heat generation of 0.077 μWm^{-3} for the basic rocks of the oceanic crust reported *by Wollenberg and Smith* [1987] will contribute a negligible amount (0.46 mWm^{-2} for

crust 6 km thick) to the surface heat flux and is not considered here.

Another factor that must be considered is variation in thermal conductivity with depth. Figure 2 is an index map illustrating heat flow and thermal conductivity measurement sites in the study area. Numerous measurements have been made in the adjacent Cascadia Basin and along the flanks of the Juan de Fuca Ridge [*Korgen et al.*, 1971; *Moran and Lister*, 1987], providing estimates of thermal conductivity seaward of the deformation front. East of this front, measurements are unavailable with the exception of ODP holes 891 and 892 [*Westbrook et al*., 1994]. Landward of the continental slope, offshore exploration wells provide conductivity estimates on the continental shelf. Values of 2.5 $Wm^{-1}K^{-1}$ [*Fowler*, 1990] to 2.9 $Wm^{-1}K^{-1}$ [*Turcotte and Schubert, 1982*] are common estimates of the thermal conductivity of oceanic crust (i.e., mid-ocean ridge basalt), reported in the literature. We use a value of 2.9 $Wm^{-1}K^{-1}$ to better approximate the bulk thermal conductivity of the entire slab, not just the oceanic crustal portion. It may be argued that because the thermal conductivity of most lithologies is inversely proportional to temperature [*Birch and Clark*, 1940], the thermal conductivity of basalt will decrease at depth (i.e., higher temperatures). Anticipating this decrease, we tested the effect of the lower basalt thermal conductivity, 2.5 $Wm^{-1}K^{-1}$. However, models utilizing the two thermal conductivities are almost identical (±0.5 °C), so we chose the higher value to facilitate the direct comparison of the static, wholly conductive models developed here with kinematic thermal models presented elsewhere [*McKenna and Blackwell*, manuscript in preparation].

Tréhu et al. [1995] determined the offshore structure of the northern Cascadia subduction zone near 45 °N using seismic reflection data. Figure 6b is a simplified version of this structure, illustrating the model geometry. The accretionary complex is composed of fine-grained sediments (shales and mudstones) and is about 2 km thick near the deformation front. It thickens

eastward to about 14 km near the edge of the Siletz Terrain. The oceanic crust is unimaged by reflection data within the accretionary wedge, but assumed to have a constant thickness of 6 km (dashed line, Figure 6b). Most oceanic thermal conductivity estimates in this area on unconsolidated sediments present to about 25 km east of the deformation front are between 0.76-1.0 $Wm^{-1}K^{-1}$ [e.g., *Korgen,* 1971*; Moran and Lister*, 1987; *Westbrook et al*., 1994; *Lyle et al*., 1997] hence we use a thermal conductivity of 0.9 $Wm^{-1}K^{-1}$ for the uppermost 0.5 km of sediments (i.e., above the solid line in Figure 6a). A substantially higher thermal conductivity (1.37 $Wm^{-1}K^{-1}$) is appropriate for the first 5 km starting about 25 km landward of the deformation front (i.e., the sediments above the dash-dotted line in Figure 6a). This is most likely due to fluid expulsion and compaction at greater depths, the effect of which is to decrease *in-situ* porosity that in turn, increases the *in-situ* thermal conductivity. Because the porosity loss and hence, change in thermal conductivity are not known, the thermal conductivity of the deeper sediments within the accretionary wedge between the aforementioned first layers and the subducting oceanic lithosphere was simply assumed to be 2.0 $Wm^{-1}K^{-1}$. Additionally, a change in both thermal conductivity and heat generation of the Siltez backstop above and below 5 km (refer to Figure 6b) are incorporated into the model to accommodate a probable change in the thermal conductivity, and possibly heat generation of this unit at depth. The thermal parameters for this and the other units that comprise the northern Oregon model are summarized in Table 3.

Northern California Thermal Models

Thermal parameters along the northern California profiles are less certain than those utilized in constructing the northern Oregon profile, primarily because of the lack of offshore drilling, and incomplete published data. Most data available are from onshore heat flow/thermal conductivity measurements. The most westerly of the two offshore ODP heat flow

measurements (site 1020, 44 km west of the deformation front) has such a large uncertainty (± 26 mWm^{-2}) that effectively, no offshore data may be used to constrain the model with a degree of certainty [*Westbrook et al*., 1994].

Structurally, the northern California cross-section is comprised of 2-3 km of sediment on 5 Ma oceanic lithosphere subducting beneath the North American Backstop composed of Mesozoic Franciscan Complex and Klamath granite overlain by a localized basin of Eel River sediments (Figure 7b) [e.g., *Smith et al*., 1993; *Verdonck and Zandt*, 1994]. The abundant accretionary material characteristic of the northern Oregon profile is lacking at this latitude, but because the plate is well covered with sediment before it enters the trench, the slab-surface temperature remains above 200 °C. Choosing the appropriate values for thermal conductivity and heat generation for the Franciscan is problematic because the lithology, and thus thermal parameters of the metasediments that compose the Franciscan are extremely variable. *Lachenbruch and Sass* [1980] reported two values for the heat generation of the Franciscan: 1.0 and 1.2 μWm^{-3}. We use the average of these two values (1.1 μWm^{-3}) and assume that this value is representative of the upper 10 km of the Franciscan complex. The heat generation below this depth is assumed to be zero. The thermal conductivity of Franciscan metasediments was reported *by Mase et al.* [1982] as 2.49 $Wm^{-1}K^{-1}$. While there is a large variability in bedding orientation and mineralogy within the Franciscan complex, we assume that the temperature effect on thermal conductivity [e.g., *Birch and Clark*, 1946; *Pribnow et al.*, 1996] will reduce the variability in thermal conductivity at depth. Thus a value of 2.2 $Wm^{-1}K^{-1}$ below 10 km depth is assumed in the modeling (i.e., the area of Franciscan Complex below the dash-dot line in Figure 7b.

The average thermal conductivity of the Klamath granites is 2.82 $Wm^{-1}K^{-1}$ [*Mase et al.*,

1982]. However, experimental data complied by *Birch and Clark*, [1946] and *Robertson* [1989] show that quartz igneous rocks will exhibit a large reduction in thermal conductivity as temperature increases. Quartz monzanites, similar to the Klamath granite in composition, may experience up to a 30% decrease in thermal conductivity from their room-temperature values [*Robertson*, 1989]. To model this effect, we utilized a value of 2.82 $Wm^{-1}K^{-1}$ for the Klamath granite above 5 km depth (above the dash-dot line in Figure 7b), and a thermal conductivity of 2.0 $Wm^{-1}K^{-1}$below 5 km. Heat generation in these granites is quite low; about 0.5 μWm^{-3} [unpublished data, *Blackwell*, 1970], and like most plutonic rocks, may be-characterized by an exponentially-decaying heat generation distribution $A_o \exp(-z/b)$, where A_o is the surface heat generation, and b is the depth at which A is 1/e its initial value [*Lachenbruch*, 1968; *Roy et al.*, 1968]. If a value of 10 km is used for b (typical of Cordilleran granites; see *Lachenbruch*, [1970], *Blackwell* [1971], and *Roy et al*. [1972]) then the exponentially decaying heat generation of the Klamath terrane may be approximated by a 5 km and a 9.5 km thick layer, each with a constant heat generation of 0.45 and 0.3 μWm^{-3}, respectively. The additional heat introduced by this approximation is small (~1.3 mWm^{-2}), and because it is internal heat generation well above the subducting plate-top, does not significantly impact décollement temperature estimates.

The selection of thermal parameters for the Eel River and accretionary complex sediments is somewhat arbitrary because little or no published data exists for these sediments. Furthermore, no surface heat flow data are available for the basin. *Mase et al.* [1982] reported a thermal conductivity of 1.3 $Wm^{-1}K^{-1}$and heat generation of 0.5 μWm^{-3} for "alluvium" approximately coincident with the basin containing Eel River sediments. There is most likely a refraction caused heat flow low associated with the lower thermal conductivity sediments present in the basin. Taking into account compaction effects, we utilize a somewhat higher thermal

conductivity of 2.0 $Wm^{-1}K^{-1}$, for the Eel River sediments in the modeling. Additionally, we utilized a somewhat higher than average thermal conductivity (1.81 $Wm^{-1}K^{-1}$) with respect to the Oregon accretionary complex sediments to match the observed surface heat flow near the deformation front.

RESULTS

Numerical Modeling

The two-dimensional, steady state heat equation with internal heat generation was solved using the relaxation method [e.g., *Beardsmore and Cull*, 2001] for both the northern Oregon and northern California geometries (Figures 6b and 7b, respectively) with thermal parameters listed in Table 3. For simplicity, we assume that thermal conductivity change with temperature [e.g. B*irch and Clark*, 1946] is modeled by decreasing the thermal conductivity of selected lithologies with depth by using layers in the model as discussed in a previous section. Neglecting this effect during the computation could systematically underestimate temperatures by overestimating the in-situ thermal conductivity at depth, but because we endeavor to obtain minimum temperature distributions, we deem the use of constant thermal conductivity is acceptable.

The steady-state conditions along the northern Oregon profile are justified as follows. Subduction of the Juan de Fuca plate near 40 °N has been continuous for about 40 Ma [*Riddihough*, 1984]. The characteristic thermal distance, L_T, is the distance heat will conduct over a given length of time. It is equal to $(\kappa t)^{1/2}$, where κ is the thermal diffusivity of the medium. Using the typical diffusivity for sediments, 10^{-6} m^2/s, and t = 40 Ma, L_T is roughly 36 km. Near northern Oregon, the maximum depth of modeled décollement temperature is only 27 km, well within the thermal length of the model. A similar argument cannot be made for the

northern California profile because of the transient thermal effects of the MTJ. This thermal effect is commonly referred to as "the hole in the plate" [e.g., *Lachenbruch and Sass*, 1980]. However, because we are modeling north of the triple junction, the transient effects discussed above are avoided, and our steady-state assumption remains valid.

The finite-difference grid spacing utilized was 2.5 km in the horizontal (x) direction and 0.5 km in the vertical (z) direction. We specified three boundary conditions for the models. First, the surface temperature was assumed to be 0 °C along the seafloor and 10 °C on the continental shelf and onshore portions of the model. Second, the vertical heat flux from the slip zone, q_m is calculated from the fit to the observed surface heat flow profiles (solid lines, Figures 6a and 7a) by subtracting the heat generation contribution from sediments present within the accretionary complex. The third boundary condition specified was the vertical temperature distribution in the incoming plate at -30 km and –44 km (northern Oregon, and northern California, respectively). We determined the one-dimensional temperature profile by first specifying the slab-surface temperature from the age-dependent heat flow and linearly interpolating this temperature to 0 °C upwards through the sediment column, and finally, utilizing an error function solution from the slab-surface temperature, until the base of the slab is reached at 30 km depth.

Wang et al. [1995b] stress the importance of determining the appropriate thermal history of the incoming plate (i.e., sedimentation and fluid migration) to properly specify this boundary condition. However, the only effect of increasing/decreasing the slab temperature in the static models developed here is to raise/lower the calculated surface heat flow in the first 20 km or so of the model, an area that we are not concerned with in this study. The implications of varying the slab-surface temperature for the static models are illustrated in Appendix 2. Here we merely

note that slab surface temperatures of 200 °C and 250 °C were used to develop the boundary condition at 0 km for both northern Oregon, and northern California, respectively.

Temperature Profiles

To investigate the effect of different surface heat flow values on the deeper thermal structure, we discuss two thermal models, one corresponding to the "low" heat flow curve fit to the observed data, and the other model corresponding to the "high" heat flow curve. Otherwise, identical model parameters were utilized. The contoured two-dimensional steady-state temperature output and the calculated surface heat flow profile corresponding to the "low" heat flow northern Oregon model are shown in Figure 8b, whereas the "high" heat flow model isotherms are shown in Figure 8c (Figures 9b and 9c show the corresponding northern California model). The calculated heat flow profile for the different heat flow basal conditions appear in Figures 8a and 9a for northern Oregon, and northern California, respectively. In all cases beginning about 25 km east of the deformation front, the thermal models fit the observed heat flow data. Seaward of the deformation front where the heat flow is not well known the models do not fit the observed data as well.

Although no variations in thermal conductivity and heat generation are present between the two models, the effect of the different basal heat flow condition is apparent. From 0-25 km the two models are within 50 °C of one another. By a distance of 25 km east of the deformation front, however, the basal heat flow assumption begins to affect the shape of the isotherms more dramatically. The temperature difference between the two models reaches a maximum of 64 °C by about 8.6 km depth, or 30 km east of the deformation front.

The thermal cross-sections that best represent the northern California profile are presented in Figures 9b and 9c. The significant difference between the two surface heat flow

curves used to construct the basal heat flow boundary conditions for the two models generates temperature profiles that are very different. Because the offshore heat flow is almost totally unconstrained until 40 km east of the deformation front, the thermal structure for a large portion of the distance from the deformation front to the coast is subject to large uncertainties. The maximum difference between the high heat flow and low heat flow northern California models is 117 °C at 10.3 km depth, about halfway between the deformation front and the coast (Figures 9b and 9c).

The calculated surface heat flow profiles for both the northern Oregon and northern California temperature models satisfy the observed heat flow data. The good fit to the data at, and especially landward of the deformation front, supports our use of wholly conductive models to estimate décollement thermal conditions.

Although the thermal parameters used in this study to characterize the oceanic sediments and deeper accretionary sediments are comparable to those used by *Hyndman and Wang* [1993] in modeling subduction zone thermal processes along the Cascadia margin, we assessed the dependency of the model results on particular values of these parameters by varying them within their typically encountered range (Appendix 1). Overall, the models results did not change substantially, but did yield a range of décollement temperatures which helped to constrain the maximum errors associated with the modeling, the results of which will be discussed in a later section.

The range of possible thermal parameters utilized in the modeling of the northern California area are much less constrained than those of the northern Oregon area and hence, are of limited use in deriving end-member thermal models. The most plausible variation of thermal parameters that we envisage generating significant thermal effects is an anisotropic thermal

conductivity structure in the Franciscan Complex. We investigated this possibility by utilizing a vertical/horizontal thermal conductivity ratio of 1.25, but determined that the overall effect on décollement temperature is minor (Appendix 1). Furthermore, we have checked our wholly conductive models against transient two-dimensional kinematic finite element models (see Appendix 2), which show that décollement thermal conditions presented in this study are very similar to the results obtained from more sophisticated numerical modeling.

DISCUSSION

Décollement Thermo-Mechanical Conditions

The complete thermal cross-sections generated above are useful for visualizing the Cascadia forearc subduction zone thermal regime. The only two heat sources within the wedge are the relatively well-constrained (by geophysical well-logs and laboratory analysis) internal heat generation of the accretionary prism and backstop, and the basal heat-input from the subducting lithosphere. If the sum of these two contributions is less than the observed heat flow at any point, there must be an additional, unspecified contribution. Brittle shear heating is usually incorporated into subduction zone thermal models to explain this deficit [*Molnar and England*, 1990; *Peacock*, 1993; *Peacock and Wang*, 1999]. However, brittle shear heating is not modeled as a source of heat for either model nor for most subduction zones. In fact, surface heat flow profiles constructed (in a forward sense) from the accretionary wedge/backstop heat generation and an age-dependent, basal heat-input (i.e., equation (4)) generate heat flow values that are up to four times larger than those actually observed.

However, the focus in this discussion is on the insight into present-day Cascadia plate boundary fault strength and metamorphic conditions provided by our analysis of the thermal conditions experienced by the décollement. In order to define the thermal conditions, the

position of the main thrust of the subduction zone must be estimated. Studies by *Smith et al.* [1993] suggest the décollement in northern California is the oceanic crust-Franciscan Complex boundary (Figure 8). The position of the décollement along the northern Oregon profile is not as readily identified.

Numerous studies detailing the shallow structure [*MacKay et al.*, 1992; *Moore, et al.*, 1995; *Tréhu et al.*, 1994; *Tréhu et al.*, 1995] exist, but no deep reflections imaging either oceanic crust or the basal thrust have been observed deep within the accretionary complex (e.g*., Tréhu et al.*, 1995]. Modeling is simplified if the oceanic crust is assumed to be of uniform thickness within the subduction complex (Figure 7). The position of the décollement is, however, a matter of interpretation. Using refraction data, *MacKay et al.* [1992] placed the décollement at about 1.3 km above the base of the sediment column just landward of the deformation front. Farther east the position of the décollement is unknown, but is assumed to level out, merging with the oceanic crust-sediment column boundary about 8 km farther east. Ideally, earthquake hypocenter data could be used to delineate the basal thrust, but such data do not exist here. We therefore assume that no sediment is underthrust, and that from about 8 km east of the deformation front, the décollement is the oceanic crust/sediment interface. It is noted that a shallower décollement will experience low temperatures [e.g., *Hyndman and Wang*, 1993].

Steady-state temperature-slab-top depth curves, generated by sampling décollement temperature from both minimum and maximum temperature cross-sections of northern Oregon and northern California are shown in Figure 10. All curves (with the exception of the northern California low heat flow model) depict a large temperature gradient up to about 10 km décollement depth, a lower gradient from 10-17 km, and finally, an interval of higher temperature gradient from about 17 km to the total modeled depth. The northern California low

heat flow model temperature-depth curve is approximately linear over the entire model.

The difference between the northern Oregon décollement temperatures is readily explained by the different basal heat flow condition utilized. In spite of the uncertainty in heat flow, the models are not very different. We restrict further analysis of thermal conditions of the northern Oregon cross-section to the low heat flow model, thereby ensuring that the minimum temperature estimate is utilized. However, it is apparent that the differences between the northern California décollement temperature estimates can be quite large, depending upon which heat flow model is used. Because the theoretical heat flow at the deformation should be about three times the nearest observed oceanic measurement (ODP site 1019), the low heat flow model based on this ODP measurement is probably unrealistically low. Therefore, in subsequent sections we utilize the northern California high heat flow model.

Using *Byerlee's* [1978] frictional slip criteria, the differential stress, $\Delta\sigma$, necessary to initiate brittle failure along a cohesionless thrust fault, dipping 10° is:

$$\Delta\sigma = 5.8\ [\ \sigma_3 - \lambda\ P_v\ ], \qquad \Delta\sigma < \ 170/(1-\lambda P_v)\ \text{MPa} \tag{5a}$$

$$\Delta\sigma = 3.9\ [\ \sigma_3 - \lambda\ P_v\ ] + 392, \qquad \Delta\sigma < \ 170/(1-\lambda P_v)\ \text{MPa}, \tag{5b}$$

where the vertical stress, σ_3, is proportional to lithostatic load, P_v is the overburden pressure, and λ is the pore-fluid ratio. The power-law creep equation that governs ductile behavior [e.g., *Kirby*, 1983] is:

$$\Delta\sigma = \left[\frac{\dot{\varepsilon}}{A}\ exp\left(Q/RT \right) \right]^{1/n}, \tag{6}$$

which states that the differential stress necessary to cause ductile flow in a particular lithology is a function of temperature (T), strain rate ($\dot{\varepsilon}$), a material parameter (A), and activation energy

(*Q*). Equations (5a) and (5b*)* constrain the brittle portion of the yield-strength envelope, while the ductile segment (equation (6)) is modeled using a power-law creep equation [e.g., *Kohlstedt et al*., 1995].

Placing the décollement at the presumed base of the sediment column for the entire length of the subducting slab subjects the basal thrust to the highest temperatures within the complex and provides an estimate of the minimum differential stress (lower bound) that will cause ductile flow for various rheologies. Yield-strength envelopes using flow-law data for quartzo-feldspathic rheologies (appropriate to subduction zones) may be constructed from these temperature profiles, providing an estimate of décollement strength as a function of down-dip depth.

Equations (5) and (6) were used to construct yield strength envelopes for the sediment-oceanic crust décollement (Figures 10 and 11) using the décollement temperature (Figure 9) and a strain rate of 10^{-15} s^{-1}. Both the northern Oregon and northern California décollements are approximated by fault planes striking about 176.5° and dipping at 13° (see Figures 2, 6b, and 7b). Strength estimates obtained in this manner, however, will not accurately describe steady-state décollement conditions because σ_1 is margin-parallel (N-S), and not oriented orthogonally to the trench [*Wang et al.*, 1995, and references therein]. In this configuration, the maximum compressive stresses create a stress field that results in strike-slip, rather than thrust faulting [e.g., *Anderson*, 1951], and thus, only describe décollement conditions just proceeding and just following subduction thrust events [*Dragert et al.*, 1994]. However, because $\sigma_1 > \sigma_2 = \sigma_3$ [e.g., *Wang,* 1995], $\Delta\sigma$ is nearly identical for strike-slip faults (σ_2 vertical), and thrust faults (σ_3 vertical) so long as σ_1 remains horizontal. The only difference between the two stress regimes is that the angle between σ_1 and the normal to the fault plane changes. *Goldfinger et al.* [1997]

mapped several NNW trending left-lateral strike-slip faults along the Cascadia margin. These strike-slip faults are thought to represent the inter-seismic stress regime and are hypothesized to be a result of a margin normal σ_1. Because such strike-slip faults may better represent part of the interseismic steady-state stress conditions within the Cascadia subduction zone, we calculated strength envelopes utilizing the actual modeled décollement for both a strike-slip fault ($\phi = 176.5°$ and $\delta = 13°$), and a thrust fault ($\delta = 13°$) for both study areas (Figures 11 and 12), but only show the envelopes for the latter conditions as the results are nearly identical. Furthermore, although the time-scale appropriate for different regions along strike is probably different, we use the same strain-rate for both the northern Oregon and northern California profiles so that we may compare the strength envelopes directly.

Strength along the northern Oregon décollement using the décollement temperature obtained from the low heat flow temperature model is shown in Figure 11, and along the northern California décollement utilizing the high heat flow décollement temperature in Figure 12. The strength envelopes for wet/dry quartzite and wet/dry granite for both regions are similar, however, the diabase based strength for northern Oregon is much larger than that of northern California, simply because the initial temperature is about 50 °C cooler. Strength envelopes are only semi-quantitative conceptual devices, but they provide a convenient visualization of the effects of temperatures on relative décollement strength. Strength envelopes have been used extensively by numerous authors to impose constraints on lithospheric strength from experimental data [e.g., *Kohlstedt et al.*, 1995] and seismogenesis [e.g., *Sibson*, 1983]. Our goal by presenting both visualizations is to illustrate the effect of the unique Cascadia décollement thermal conditions, regardless of the current stress regime.

Integrated strength is another way to summarize the mechanical (both brittle and ductile)

conditions along different subduction zone faults. It is obtained by simply integrating $\Delta\sigma$ over some depth range, and thus provides a single value that is diagnostic of the particular subduction zone. The integrated fault strength for wet quartzite and diabase rheologies and both fault types through a décollement depth of 23 km are presented in Table 4. For comparison, the integrated strength of the southern Mexico and northeastern Japan subduction zones are shown. In all cases, the integrated strength of a diabase is large, indicating that even though décollement temperatures are high, a diabase rheology remains strong in the upper 20 km of the Cascadia subduction zone. In fact, the CSZ integrated strength values for a diabase rheology are 3-8 and 5-14 times smaller than those obtained from the much colder and seismically active southern Mexico and northeastern Japan subduction zones, respectively (see Table 4). However, if fault strength is limited by the weakest participating rheology [i.e. quartz; *Scholz*, 1990] the décollement is unable to support differential stress below about 5.0 km of décollement depth, regardless of which fault type is used, and the CSZ wet quartzite integrated strengths are 9-24 and 26-79 times lower than southern Mexico and northeastern Japan, respectively.

In addition to the thermal dependence on fault strength, elevated pore-fluid pressures also significantly effect décollement strength [*von Huene and Homa*, 1982]. The previous discussion assumed zero pore-fluid pressure, and is therefore an end-member evaluation of décollement strength. In fact, pore fluid pressure is often observed to approach lithostatic in accretionary prisms; pore pressures in the Oregon décollement have been observed to approach 75% lithostatic [*Wang et al.*, 1995]. This suggests the integrated strength estimates presented in Table 4 are too high, perhaps as much as 50% higher than actual *in situ* strength.

However, because relative pore pressure and stress conditions are likely to be similar from subduction zone to subduction, the relative strengths for any given set of conditions may be

compared. Thus it is clear that the Cascadia subduction zone is very, very weak compared to other subduction zones. Furthermore this weakness is primarily due to the high initial temperature of the top of the ocean crust as suggested by *Blackwell and Eckhardt* [1991], not due to the young age of the lithosphere that is being subducted. For example, the northeastern Japan subduction zone possess an integrated strength between 36-63 x 10^{12} Nm^{-1} depending on the rheology modeled, or the pore-fluid pressure present (assuming the slab temperature with depth is similar to that of *Peacock and Hyndman* [2001]) which is at least a factor of 26 times higher than the CSZ. Therefore the more analogous subduction zone settings suitable to comparison with Cascadia may be areas of thickly sedimented ocean plates and not young subduction zones *per se*. For example, as a section is drawn from south to north along the Lesser Antilles subduction zone thrust earthquakes only appear north of the area where the subducting cold North American plate is covered by thick sediment from the Orinoco River [*Stein et al*., 1983]. Also, where young lithosphere with thin sediment cover is being subducted in the Middle American Subduction zone, for example, there are large thrust earthquakes [e.g., *Suarez et al*., 1990; *Pardo and Suarez*, 1995]. Because the CSZ possesses both a thin plate and high surface temperature it is not surprising that it behaves in a very different manner. Hence, the analogy that the CSZ may be very similar to the subduction in Chile, where young Nazca lithosphere with thin sediment is being subducted beneath the South American plate [e.g., *Heaton and Kanamori*, 1984; *Heaton and Hartzell*, 1987] may not be appropriate.

P-T Paths

Another useful visualization of the distinctness of Cascadia thermal conditions is pressure-temperature (P-T) along the décollement paths [e.g., *Ernst*, 1988]. Exhumed blueschist packages, rocks characteristic of high P/T ratios, are representative of underplated or accreted

sediments and oceanic crust and mantle in subduction zones, and are commonly used to infer in situ shallow thermal conditions [*Ernst*, 1988]. Figure 13 illustrates steady-state P-T conditions in the Cascadia subduction zone superposed on a metamorphic facies diagram appropriate for oceanic crust [e.g., *Peacock*, 1993]. Also plotted for comparison, is a P-T path representative of present thermal conditions in the Sierra Nevada subduction zone (dotted line; [*McKenna*, 1997]). The Sierra Nevada P-T path is presented in the context of a paleosubduction zone that generated blueschist facies rocks in the Franciscan outer arc block [*Blackwell*, 1971].

Conditions along the Cascadia décollement do not fall within the blueschist facies stability field as might be expected because the P/T ratio is too low. Instead, the high temperatures at lower pressure push the Cascadia P-T paths into the greenschist facies, and ultimately amphibolite facies stability fields. In fact, blueschist facies P-T conditions are not predicted anywhere along the Cascadia décollement. The Sierra Nevada path probably reflects the thermally enhanced present conditions (i.e., the P/T ratio is actually lower today, than when the blueschist of the Franciscan was generated). Even so, the Sierra Nevada P/T ratio is much higher than the Cascadia P/T ratio. The results of the modeling, however, clearly show that the current formation of blueschist assemblages along the Cascadia margin is unlikely. Moreover, as younger and younger lithosphere is subducted, décollement conditions will become even less favorable for blueschist generation (assuming some sediment cover on the incoming plate). It is not clear whether or not the lower seismic velocities associated with greenschist and amphibolite (as opposed to blueschist, [*Rudnick and Fountain*, 1995]) are present within either the northern Oregon, or northern California forearcs [e.g., *Tréhu et al.*, 1994; *Smith et al.*, 1993], and can thus help calibrate the P-T analysis presented here.

To further illustrate this point, we present P-T paths utilizing the same temperature inputs

described earlier, but instead of taking pressure as simply the overburden, we increase the overburden by adding tectonic loading (Figure 14). That is, pressure is now assumed to be the average of margin normal tectonic loading (σ_1) and the overburden (σ_3). So only with the introduction of tectonic loading can P-T paths enter the blueschist facies stability field. However, if σ_1 is margin-parallel as discussed above, and not margin-normal, tectonic loading is better represented by σ_2. But because $\sigma_2 \approx \sigma_3$, pressure is actually just the overburden, returning it to its initial lower value, and eliminating the possibility of the Cascadia décollement lying within the blueschist facies stability field.

The unusual metamorphic conditions are a result of an initial décollement temperature of at least 200 °C at very shallow depths. Both the northern Oregon and northern California P-T paths have an initial slope of about 1.5 MPa/°C, placing them in the greenschist and amphibolite stability field. From here the P-T ratio rapidly increases as the temperature gradient begins to decrease. Unfortunately, our model calculations do not extend beyond this depth and we do not predict the pressure-dependent amphibolite → eclogite or temperature-dependent glaucophane + lawsonite → eclogite transition (i.e., blueschist → eclogite transition; [*Peacock*, 1993]) explicitly. However, it is commonly held [e.g*., Davies and Stevenson*, 1992] that the most important source of slab-derived fluids fluxing the mantle wedge (i.e., responsible for arc-volcanism) is the amphibolite → eclogite dehydration reaction. *Kirby et al.* [1996] have proposed that this dehydration reaction creates a densification (volume change) within the subducting oceanic crust, which may be responsible for intermediate depth seismicity. Furthermore, if the slab passes through the blueschist→ eclogite reaction, several hydrous phases, and therefore substantial quantities of fluids, are transported to great depths (80-100 km), as opposed to being liberated at shallower (~ 45 km) depths [*Kirby et al.*, 1996].

The average Cascadia (of all plotted P-T paths) path terminates at about 510 °C and 706 MPa (~27 km). Beginning near 45 km depth the subducting oceanic crust will begin to transform to eclogite. The (average) Cascadia P-T path can pass through one of two reactions to begin this transformation: the pressure-dependent (quasi-isothermal) or temperature-dependent (quasi-isobaric) path (both shaded in Figures 13 and 14). Although the slab face is relatively hot at this depth, it will need to heat up an additional ~ 70 °C over the next 18 km to begin the amphibolite → eclogite transition. This requires (assuming a linear increase in temperature) a gradient of about 4 °C/km. Both northern Oregon and northern California models terminate with a décollement temperature gradient of about 15 °C/km. If no other sinks/sources are present, the slab face should pass through the pressure-dependent amphibolite → eclogite reaction at about 45 km depth. Any derived fluids from this reaction would not enter the mantle wedge deep enough to be in a position to generate arc-volcanism, possibly supporting the *Kirby et al.* [1996] observation of feeble, or non-existent arc-volcanism associated with the subduction of young slabs. Recent thermal modeling of the young, thickly sedimented southwestern Japan subduction zone has provided similar results to those presented here: the décollement passes through the greenschist, then epidote-amphibolite, and finally, through the pressure-dependent transition to eclogite [*Peacock and Wang*, 1999].

The modeled P-T paths most similar to the *Peacock and Wang* [1999] results are those calculated with tectonic loading (i.e., pressure is the average of the principle stresses). If the pressure determined in this manner is accurate, temperature increases slowly with respect to pressure, suggesting that the slab face does not appreciably heat-up as it descends. If the slab follows this path, it will transform to eclogite via the temperature-dependent blueschist → eclogite transition (Figure 14). This would require an almost isothermal P-T path from 27-45

km. There is no reasonable mechanism that would cause the temperature gradient to suddenly drop to near zero and furthermore, the volcanic-arc is still ~100 km to the east of the termination of the model. From this we conclude a nearly isothermal P-T path possible, if the inclusion of tectonic loading in the pressure term is appropriate.

CONCLUSIONS

We have presented a method for modeling décollement thermal conditions in shallow subduction zones by specifying the heat flux from the subducting slab into the overlying accretionary complex and backstop. New data from six offshore and two onshore oil wells located on the Oregon margin (mean 39.8 $\pm$ 5.1 mWm^{-2}) and a theoretical heat flow at the deformation front constrain the observed surface heat flow profile. The new and previously published heat flow values provide the basal boundary condition, after removal of the effects of heat production, used in subsequent modeling. A similar methodology is used to model the even younger Gorda slab subducting north of the Mendocino Triple Junction.

Satisfying the basal heat flow boundary condition in this manner eliminates the need to specify the deep, unconstrained thermal structure of the subducting slab to obtain a solution, reduces the vertical scale of the model (i.e., by solving the problem above the décollement), it obviates the necessity of including any possible deep (mantle) convection, and automatically satisfies the observed surface profile. Thus this approach demonstrates the advantage of using the surface heat flow to accurately constrain the thermal regime of the subduction interface in contrast to most approaches which start with the less well known and less well constrained deep effects and thus have errors that are difficult to evaluate and constrain and may not generate realistic surface heat flow distributions.

Results from numerical models in northern Oregon and northern California reveal two

distinct décollement thermal regimes: the shallow (upper ~10 km) segment of the décollement that experiences unusually high temperatures, and the deeper, lower thermal gradient décollement adjacent to the backstop. The first thermal regime exists as a consequence of the insulating sediment cover near the deformation front. If the slab is not devoid of sediment cover, the décollement will attain high temperatures at shallow depth because it heats up from an initial temperature of ~200 °C, instead of the much colder temperature of the surrounding ocean water (i.e., 0 °C). Furthermore, if the subducting slab is relatively flat, the thermal gradient along the shallow segment of décollement is initially very large as the temperature in the upper ~10 km rapidly changes from 0-200 °C. Once this segment of the décollement is passed, the temperature gradient drops to the much lower value of ~6 °C/km, because most of the heat input into the forearc at this point in the model is internal heat generation, and not heat from the subducting slab.

Temperatures in excess of 350 °C are attained by ~16 km depth for the northern Oregon model, and ~11 km depth for northern California. This temperature is a maximum of about 50-75 km east of the deformation front in northern Oregon, and about 30 km east of the deformation front in northern California (Figure 10b). This temperature is commonly thought to represent the beginning of quartz plasticity, and is therefore the temperature limit to seismogenesis. At 450 °C, feldspar begins the transition to plasticity, and should no longer be seismogenic. This temperature occurs at about 22 km depth for both modeled area. In northern Oregon this corresponds to 105 km east of the deformation front, while in northern California, this temperature is reached about 90-95 km east of the deformation front, depending on which heat flow model is utilized. These estimates are similar to those reported for this region and that to the north [*Hyndman and Wang* 1993; *Hyndman and Wang* 1995; *Oleskevich et al*., 1999]. Our

slightly wider estimates from these locations arise from comparable, but somewhat different modeling parameters, and our approach utilizing the minimum temperature estimates obtained from our modeling.

Because little seismicity is present along the Oregon corridor of the CSZ, we cannot compare our results directly with earthquake distribution, so instead, we do so for the northern California profile. The down-dip seismogenic segment of the décollement is between the 150 and 350 °C isotherms, or the temperature at which quartz minerals exhibit stick-slip behavior. This corresponds to *Hyndman and Wang's* [1993] "locked" zone, the zone from 350-450 °C, or the temperature at which feldspar begins to deform ductilely, but may still exhibit semi-brittle behavior is their while seismogenic "transition" zone. Despite the uncertainties in our temperature estimates for the northern California profile, and the hypocentral depth determinations for this profile, the absence of earthquake activity along the décollement begins at about 350 °C (Figure 15). At temperatures higher than 450 °C, the décollement is hypothesized to exhibit stable sliding characteristics (e.g., *Hyndman and Wang's* [1993] "free-slip" zone, see Figure 10b), and should therefore be aseismic. We observe that décollement seismicity does tend to cease above this temperature. Earthquakes do occur at temperatures higher than 450 °C, however, they occur in the subducting Juan de Fuca oceanic crust and mantle, a segment of the slab governed by a much stronger rheology (i.e., olivine). The hypocenters that cluster about 20-30 km depth are Mendocino Triple Junction events from south of the profile, and are not useful in correlating seismicity with temperature. Note that just above the intersection of the 350 °C isotherm with the décollement, the 1992 Petrolia (M_s~7.1) earthquake occurred around ~15 km depth [e.g., *Oppenheimer et al*., 1992], suggesting that the absence of aftershock activity near this depth may be a consequence of the high décollement e

temperature.

The maximum seismogenic widths listed above that suggest that large earthquakes may occur along the middle and southern segment of the Cascadia subduction zone. However, from the P-T analysis, it is clear that the shallow décollement is rather unusual; the large rapid, temperature increase that both areas experience generates pressure-temperature conditions suitable for shallow greenschist and amphibolite facies metamorphic conditions, and not blueschist facies formation. The Cascadia subduction zone is hypothesized to generate $M_w \sim 9.0$ thrust events [e.g., *Hyndman and Wang*, 1993]. From the strength envelope analysis, the décollement approaches low strength at very shallow depths, suggesting that the décollement cannot sustain differential stress and is thus, aseismic. However, because the décollement temperature is buffered between 350-500 °C, the subduction thrust zone may maintain a finite strength in the "ductile" regime and may accommodate the rapid, aseismic slip observed elsewhere within the Cascadia subduction zone [e.g., *Dragert et al*., 2001].

Acknowledgments

We would like to thank Dick Bowen for the BHT data and geophysical logs for the wells reported in this study, Kris Eckhardt for some of the initial analysis, Graeme Beardsmore, and Kelin Wang for the use of their modeling programs. Earthquake hypocenters were obtained from the online UCB and NCSN catalogs.

APPENDIX 1

In order to asses the model dependency on the thermal conductivity and heat generation of the deepest accretionary wedge sediment and backstop (beginning at a distance of 25 km, 5 km depth Figure 6) in the northern Oregon profile, models were generated spanning the likely range of these parameters (2.0-2.25 $Wm^{-1}K^{-1}$, and 0.43-0.65 μWm^{-3}). Utilizing 2.25 $Wm^{-1}K^{-1}$ as the thermal conductivity and 0.65 μWm^{-3} as the heat generation for this portion of the model (sediments > 5 km) as opposed to the preferred values appearing in Table 3 results in a décollement temperature that is a maximum of 25 °C lower, especially apparent in the depth range of 10-15 km (corresponding to the base of the Siletz terrain) for both the low and high heat flow models. The decrease in décollement temperature is not unexpected because as the thickness of sediment in the accretionary complex increases, and conductivity and heat generation variations become more important and the isotherms of the colder model are more depressed relative to the hot model. Models using a lower thermal conductivity of 2.5 $Wm^{-1}K^{-1}$ for the subducting oceanic crust were also created for the different heat flow models. Because the modeling procedure is insensitive to the effects of the subducting slab, the calculated thermal structure remains the same. Given the minor changes to the model incurred by the significant range of values employed, we conclude that the northern Oregon thermal model is relatively insensitive to the particular thermal conductivity and heat generation values chosen to represent the various model lithologies.

To test the northern California model sensitivity we explored the two primary unknowns in our models: the thermal conductivity structure in the Franciscan Terrain, and constant, as opposed to exponentially decaying, heat generation in the Klamath granite. The surface values of thermal conductivity and heat generation for the northern California lithologies are relatively

well constrained through drilling and laboratory measurements [*Lachenbruch and Sass*, 1980; *Mase et al*., 1982]. It is uncertain, however, how these properties vary with depth.

Thermal conductivity anisotropy in the Franciscan is difficult to evaluate, primarily because the orientation of the bedding is extremely variable. Nonetheless, we investigated the effect of moderate thermal conductivity anisotropy on the calculated thermal regime. As expected, both high and low heat flow models that utilized a lower horizontal thermal conductivity (K_h = 2.0 $Wm^{-1}K^{-1}$, < 10 km; K_h = 1.76 $Wm^{-1}K^{-1}$, > 10 km) resulted in higher temperatures. The temperature differences between these models and those utilizing an isotropic Franciscan thermal conductivity ($K_z = K_h$ = 2.49 $Wm^{-1}K^{-1}$< 10 km; $K_z = K_h$ = 2.49 $Wm^{-1}K^{-1}$> 10 km), resulted in negligible temperature differences (less than 6 °C). Although a slight temperature difference is present, the décollement temperature depth curves are practically identical for models with and without thermal conductivity anisotropy. It is concluded that the horizontal conduction of heat is not important here, or in other subduction zones of shallow dip, simply because the bulk of heat-transport is vertical (i.e., one-dimensional, see *Molnar and England* [1995]).

The other thermal property variation investigated is the effect of the heat generation distribution within the Klamath granite. The Klamath granite attains a maximum thickness of 14.5 km near the eastern edge of the profile [*Smith et al.*, 1993]. Assuming a constant heat generation (A_o) within this lithology results in 7.25 mWm^{-2} of internal heating. The contribution of an exponentially decreasing heat generation distribution ($A_o \exp[-z/b]$) over an equivalent thickness is 3.8 mWm^{-2}. Here, b = 10 km, and is the depth at which heat generation attains 1/e of its surface value, A_o. Because the difference between the two distributions is minor, and more importantly, is added to the model substantially above the décollement, it

matters little whether a constant, or exponentially decreasing distribution is utilized. However, we choose to approximate the exponentially decreasing distribution with two layers of 5 and 9.5 km thickness (0.45 μWm^{-3}, and 0.3 μWm^{-3}, respectively).

We also compared the calculated surface heat flow obtained from the models described above with those created utilizing the parameters given in Table 3. Because the temperature profiles are almost identical, the surface heat flows from the models are also very similar. Differences are apparent for the northern Oregon models, especially between the deformation front and coast where the accretionary material is thickest, but are no more so than 2 mWm^{-2}. Elsewhere along the northern Oregon sections, and everywhere along the northern California sections the calculated surface heat flow is identical between the preferred models discussed in the text, and the models referred to above.

APPENDIX 2

The importance of creating simple, yet accurate subduction zone thermal models that are primarily constrained by surface heat flow measurements has prompted the present work. However, in order to assess the appropriateness of our choice of modeling technique we have created identical two dimensional conduction/advection models (see *Hyndman and Wang* [1993] for an explanation of the numerical model) to compare with the wholly conductive thermal models developed and discussed in the text. For northern Oregon, a steady-state kinematic thermal model was constructed that was as similar as possible to the conductive model structure appearing in Figure 6, utilizing a subducting slab velocity of 33 mm/yr, and thermal parameters identical to those listed in Table 3. No major difference between the two models exists. Figure A1 is the slab-top temperature as function of depth. Seaward of the deformation from where the influence of the slab velocity is greatest, a 200 °C slab-top (before it enters the trench) kinematic model is about 25 °C greater than the low heat flow conductive model. Within the accretionary complex however, the kinematic model is cooler than this model by about 30 °C at 8.5 km depth, reaching a maximum of 85 °C colder by the maximum modeled conductive depth. If the slab-top temperature is 350 °C before it enters the trench, then the northern Oregon high heat flow model is nowhere more than about 45 °C different from the kinematic model.

The northern California conductive thermal models were similarly compared to kinematic models. The northern California kinematic models utilizing a subducting slab velocity of 40 mm/yr, and thermal parameters identical to those listed in Table 3 for a 250 and 350 °C slab-top temperature are also plotted in Figure A1. The northern California low heat flow conductive model, previously rejected because it yielded décollement temperatures that were unreasonably low, is also much colder than the identical kinematic model. However, the high heat flow

conductive model is quite similar to the 350 °C slab-top kinematic model, attaining a maximum temperature difference of only 30 °C.

Comparing the calculated surface heat flow obtained from the conductive models with those created utilizing the kinematic parameters given described above yielded an excellent match east of the deformation front. However, seaward of the deformation front where the heat flow is unsure (northern Oregon), or unknown (northern California), the two modeling procedures yield much different calculated heat flow curves. But because the actual thermal regime of the subducting slab in this region is not important for this study, we feel that the conductive models described above for the wedge are robust, and as valid as those that incorporate advective heat-transfer along the base of the wedge.

FIGURE CAPTIONS

Figure 1. Tectonic index map (barbed line) of the Pacific Northwest. The general absence of seismic activity between the deformation front and the volcanic arc (triangles) to the east is obvious. Events near the Mendocino Triple Junction less than 4.5 in magnitude have been removed for clarity. Hypocenters courtesy of the National Earthquake Information Center (NEIC) and the Council of the National Seismic System (CNSS).

Figure 2. Heat flow and site index map of the Pacific Northwest study area. Existing heat flow data are from the Geothermal Map of North America [*Blackwell and Steele*, 1991, and references therein]. In the upper plot, exploration wells used to calculate new heat flow data are named, whereas wells that yielded BHT information only appear as unnamed well symbols (upper plot). The locations of the cross-sections of *Smith et al.* [1993] (northern California), and *Tréhu et al.* [1995] (northern Oregon) that provide structural control for the thermal models are shown as lines. Quaternary volcanoes are shown as triangles.

Figure 3a. Uncorrected bottom hole temperature (BHT) data from onshore and offshore exploration wells. Symbols refer to abbreviated well names listed in Table 1. The entire dataset is well represented by a least-squares fit fixed at a mean annual surface temperature of 10 °C.

Figure 3b Corrected bottom hole temperature (BHT) data from onshore and offshore exploration wells. Symbols are the same as in Figure 3a. With the exception of two deep measurements at 3900 m depth, all data are well represented by the least squares fit fixed a 10 °C shown. The temperature gradient has been increased by about 5 °C/km from Figure 3a.

Figure 4a. Bullard plot of the uncorrected BHT data set. The inverse slope of the Bullard plot is the heat flow, so it is important that the segments are as straight as possible. Here, the uncorrected slopes are erratic.

Figure 4b. Bullard plot of the corrected BHT data set. Application of a correction scheme results in more nearly linear segments, and thus, a better estimate of the heat flow.

Figure 5. Cartoon illustrating the (generally conductive) thermal conditions within the forearc. The only region that is affected by non-conductive process is crosshatched, and the observed surface heat flow (q_s) labeled "possibly advectively disturbed" or "disturbed". Regardless of position within model, a conductive heat flux (q_m) emanates from the subduction zone interface (dark filled region).

Figure 6. (a) Heat flow cross section for the northern Oregon study area. Existing data appear as circles (published data), filled triangles (ODP data), or data developed in this study (squares). The theoretical heat deformation front heat flow (see text for explanation) is a star. The two curves labeled "low" and "high" heat flow are the fits to the observed heat flow data, and serve as the basis for subsequent thermal modeling. (b) Structural cross-section modified from *Trehú et al.* [1995]. The top of the subducting plate (dotted line) has not been observed at depths

greater than 10 km, but is assumed to maintain a constant 6 km thickness above the base of the oceanic Moho.

Figure 7. (a) Heat flow cross section for the northern California study area. See Figure 6a and the text for and explanation of the data symbols and heat flow curves. (b) Structural cross-section (modified from *Smith et al.* [1993]) detailing the model geometry.

Figure 8. (a) Calculated surface heat flow along the northern Oregon profile and contoured temperatures based on the (b) lower heat flow model and (c) higher heat flow model. Temperature contour interval is 50 °C with a bold contour every 100 °C . At 10 km depth, the difference between the two models is about 65 °C.

Figure 9. (a) Calculated surface heat flow along the northern California profile and contoured temperatures based on the (b) lower heat flow model and (c) higher heat flow model. Temperature contour scheme is the same as that for Figure 8. The lower heat flow model yields décollement temperatures dramatically lower than the high heat flow model; by 10 km depth, the difference between the two models is about 80 °C.

Figure 10. Décollement temperature as a function of (a) depth and (b) distance from the deformation front. Temperature is sampled along the décollement beginning at 2.7 km depth. The strength classification as a function of décollement temperature is from *Hyndman and Wang* [1993]. Both the northern Oregon, and northern California décollements experience very high temperatures (and thus, large gradients) at the relatively shallow depths of 10-15 km. At greater depths, the Oregon temperature curves become roughly linear with a temperature gradient of about 20 °C/km, whereas the California models attain a final gradient of about 14 °C/km.

Figure 11. Strength along the northern Oregon décollement using the low heat flow temperature model for various rheologies. Power-law curve constants are from *Kirby* [1983]. Brittle fracture criteria is from *Byerlee* [1978]. A strain rate of 10^{-15} s^{-1} was used to construct the power-law segment. The solid lines form a strength envelope that assumes the décollement is a thrust fault (azimuth 176.5°/ dipping 13°; *Tréhu et al.* [1995]) with a pore-fluid ratio of either 0 or 0.38 (hydrostatic). Strength is not only a function of temperature (depth), but also a strong function of the pore-fluid pressure (λ). The décollement temperature extracted from the low heat flow model is also shown for reference.

Figure 12. Strength along the northern California décollement using the high heat flow temperature model for various rheologies. Parameters and references identical to Figure 11, except azimuth/dip which are from *Smith et al.* [1993].

Figure 13. Steady-state P-T conditions in the Cascadia subduction zone with $P=\sigma_v=\rho gz$. The dashed line denotes present day Sierra Nevadan pressure-temperature conditions as a proxy for Mesozoic North American margin conditions that generated the blueschists of the Franciscan Complex. The pressure-dependent and temperature-dependent basalt $\rightarrow$ eclogite transformations are both shaded. Depths were converted to pressure assuming the pressure is merely the overburden (density of 2750 kg/m^3). Note that P-T conditions are appropriate for generation of greenschist and amphibolite facies rocks along the décollement, and not the

expected blueschist facies typical of other subduction zones. The petrogenic grid (thin black lines) is from *Peacock* [1993] and references therein. Metamorphic facies abbreviations are: ZE, zeolite; PP, prehnite-pumpellyite; LC, lawsonite-chlorite; PA, pumpellyite-actinolite; GS, greenschist; EA, epidote-amphibolite; EB, epidote-blueschist; LB, lawsonite-blueschist; AM, amphibolite; EC, eclogite.

Figure 14. Steady-state P-T conditions in the Cascadia subduction zone with $P=(\sigma_1+ \sigma_3)/2$. Identical to Figure 12, except that now the pressure for all paths reflects tectonic loading. Only now do both the northern Oregon and northern California P-T conditions approach the blueschist stability field, typified by the Sierra Nevada path. Even so, both P-T paths are hotter at shallow depths than the "normal" Sierra Nevada P-T path.

Figure 15. Thermal constraints on seismogenesis along the décollement for the northern California profile. The isotherms are from the high heat flow model. The absence of earthquakes along the décollement in northern California profile seems to correlate with the 350 °C isotherm. Note that seismicity is present at higher temperatures, but is restricted to the "stronger" subducting Juan de Fuca oceanic crust and mantle. Earthquakes are from the UCB and NCSN catalogs from the period 1990-2001.

Figure A1. A comparison of décollement temperatures obtained from static finite difference (this study) and kinematic finite element thermal models (*McKenna and Blackwell*, manuscript in preparation). The modeling particulars are discussed in Appendix 2.

TABLE CAPTIONS

Table 2. Calculated heat flow in offshore and onshore industry wells. Heat generation was calculated using gamma ray well logs and equation (4) for three lithologies: claystone, 0.65 μWm^{-3}; siltstone, 0.43 μWm^{-3}; basalt, 0.17 μWm^{-3}. As discussed in the text, each well consists of some percentage of these three lithologies, the weighted average of which, appears in the "Heat Generation" column. "Last BHT" is the depth of the last BHT measurement. "No Data" refers to the thickness of missing section.

Table 3. Thermal parameters utilized in the modeling. Note that the thermal conductivity, K, is isotropic, and that the heat generation, A, is volumetric. Models incorporating an anisotropic thermal conductivity structure are virtually identical to those models without (see Appendix 2).

Table 4. Integrated décollement strength. P_f is the pore fluid ratio (0.38 is hydrostatic) utilized in constructing the strength envelope, and thus the integrated strength. See text for details regarding the orientation of the principal stress orientation, and consequently, the faulting style (i.e., thrust or strike-slip). All integrated strength calculations are from the trench (i.e., 0 km depth) to 23 km décollement depth.

REFERENCES

Adams, J., Paleoseisimicity of the Cascadia subduction zone; evidence from turbidites off the Oregon-Washington margin, *Tectonics*, 9, 569-583, 1990.

Anderson, E.M., The dynamics of faulting and dyke formation with applications to Britain, Edinburgh, Oliver and Boyd, 1951.

Atwater, B.F., Evidence for great Holocene earthquakes along the outercoast of Washington State, *Science*, 236, 942-944, 1987.

Atwater, B.F, A.R. Nelson, J.J. Clague, and others, Great-earthquake potential in Oregon and Washington; an overview of recent coastal geologic studies and their bearing on segmentation of Holocene ruptures, central Cascadia subduction zone, *Earthquake Spectra*, 11, 1-18, 1995.

Beardsmore, G.R., and J.P. Cull, *Crustal Heat flow: a guide to measurement and modeling*, Cambridge University Press, Cambridge, pp. 324, 2001.

Birch, A.F., and H. Clark, The thermal conductivity of rocks and its dependence upon temperature and composition, *Am J. Sci*., 238, 529-558, 1940.

Blackwell, D.D., Thermal structure of the continental crust, in *The Structure and Physical Properties of the Earth's Crust*, *Geophys. Monogr. Ser.*, vol 14, edited by J.H. Peacock, pp. 169-184, AGU, Washington D.C., 1971.

Blackwell, D.D., R.G. Bowen, D.A. Hull, J. Riccio, and J.L. Steele, Heat flow, arc volcanism, and subduction in Northern Oregon, *J. Geophys. Res.*, 87, 8735-8754, 1982.

Blackwell, D.D., J.L. Steele, M.K. Frohme, C.F. Murphey, G.R. Priest, G.L. Black, Heat flow in the Oregon Cascade Range and its correlation with regional gravity, Curie point depths, and geology, *J. Geophys. Res*., 95, 19475-19493, 1990a.

Blackwell, D.D., J.L. Steele, S. Kelley, M.A. Korosec, Heat flow in the State of Washington and thermal conditions in the Cascade Range *J. Geophys. Res*., 95, 19495-19516, 1990b.

Blackwell, D.D, and K. Eckhardt, Heat flow analysis of the Cascadia subduction zone (How wide is the locked zone?), paper presented at Workshop on Oregon earthquake processes, Oreg. State Univ., Corvallis, March 18, 1991.

Blackwell, D.D., J.L. Steele, and L.S. Carter, Heat flow patterns of the North American Continent: A discussion of the DNAG Geothermal Map of North America, in *Neotectonics of North America*, edited by D.B. Slemmons, E.R. Engdahl, M.D. Zoback , and D.D. Blackwell, pp. 423-436, *Geol. Soc. Am.*, 1991.

Blackwell, D.D., and J.L. Steele*, eds., The Decade of North American Geology; Geothermal*

Map of North America, scale 1:5,000,000, Geological Society of America, Denver, Co., 1992.

Brott, C.A., D.D. Blackwell, and P. Morgan, Continuation of heat flow data; a method to construct isotherms in geothermal areas, *Geophysics*, 46, 1732-1744, 1981.

Bullard, E.C., The flow of heat through the floor of the Atlantic Ocean, *Proc. R. Soc. London Ser. #A222*, 408-429, 1954.

Byerlee, J., Friction of rocks, *Pure and App. Geophys.*, 116, 615-626, 1978.

Clark, T.F., B.F. Korgen, and D.M. Best, Heat Flow in the Eastern Caribbean, *J. Geophys. Res.*, 83, 5883-5891, 1978.

Crosson, R.S., and G.C. Rogers, Review of instrumentally observed seismicity with tectonic implications for the central Cascadia subduction zone, *Seismological Res. Lett.*, *70*, 209. 1999.

Davies, J.H., D.J. Stevenson, Physical model of source region of subduction zone volcanics, *J. Geophys. Res.*, 2037-2070, 1992.

Davis, E.E., D.S. Chapman, and C.B. Forster, Observations concerning the vigor of hydrothermal circulation in young oceanic crust, *J. Geophys. Res., 101, 2927-2942, 1996.*

Davis, E.E., K. Wang, J. He, D.S. Chapman, H. Villinger, and A. Rosenberger, An unequivocal case for high Nusselt number hydrothermal convection in sediment-buried igneous oceanic crust, *Earth Palnet. Sci. Lett.*, *146*, 137-150, 1997.

Demets, C., R.G. Gordon, D.F. Argus, and S. Stein, Current plate motions, *Geophys. J. Int*., 101, 425-478, 1990.

Dragert, H., R.D. Hyndman, G.C. Rogers, K. Wang. Current deformation and the width of the seismogenic zone of the northern Cascadia subduction thrust, *J. Geophys. Res.*, 99, 653-668, 1994.

Dragert, H., K. Wang, T.S. James, A silent slip event on the deeper Cascadia subduction interface, *Science*, 292, 1525- 1528, 2001.

Ernst, W.G., Tectonic History of subduction zones inferred from retrograde blueschist P-T paths, *Geology*, 16 1081-1084, 1988.

Ferguson, I.J., G.K. Westbrook, M.G. Langseth, and G.P. Thomas, Heat flow and thermal models of the Barbados ridge accretionary complex, *J. Geophys. Res.,* 98, 4121-4142, 1993.

Forster, A., Analysis of borehole temperature data in the northwest German Basin: continuous logs versus bottom-hole temperatures, *Petroleum Sci*, 7, 241-254, 2001.

Fowler, C.M.R., *The Solid Earth: An Introduction to Global Geophysics*, pp.472 Cambridge University Press, Canada, 1990.

Funnell, R., D. Chapman, R. Allis, P. Armstrong, Thermal state of the Taranaki Basin, New Zealand, *J. Geophys. Res.,* 101, 25,197-25,216, 1996.

Gallardo, J. and D.D. Blackwell, Thermal structure of the Anadarko Basin, Oklahoma, *Bull. Amer. Assoc. Petrol. Geol*., 83, 333-361, 1999.

Goes, S, R. Govers, S. Schwartz, and K. Furlong, Three-dimensional thermal modeling for the Mendocino Triple Junction area, *Earth and Planet. Sci. Lett.,* 148, 45-57, 1997.

Goldfinger, C., L.D. Kulm, R.S. Yeats, L. McNeill, and C. Hummon, Oblique strike-slip faulting of the central Cascadia submarine forearc, *J. Geophys. Res.,* 102, 8217-8243, 1997.

Harrison, W.E., K.V. Luza, M.L Prater, and P.K. Chueng, Geothermal resource assessment of Oklahoma, *Special Publication 83-1*, Oklahoma Geological Survey, 1983.

Heaton, T.H., and Kanamori, H., Seismic potential associated with subduction in the Northwestern United States, *Bull. Seismol. Soc. Am.*, 74, 933-944, 1984.

Heaton, T.H., and S.H. Hartzell, Earthquake hazards on the Cascadia subduction zone, *Science*, 236, 162-168, 1987.

Hutchison, I., The effects of sedimentation and compaction on oceanic heat flow, *Geophys. J.R. Astron. Soc.,* 82, 439-459, 1985.

Hyndman, R.D., and K. Wang, Thermal constraints on the zone of major thrust earthquake failure: The Cascadia subduction zone, *J. Geophys. Res.*, 98, 2039-2060, 1993.

----------, The rupture zone of Cascadia great earthquakes from current defomation data and the thermal regime, *J. Geophys. Res.*, 100, 22133-22154, 1995.

Hyndman, R.D., M. Yamano, and D.A. Oleskevich, The seismogenic zone of subduction thrust faults, *The Island Arc*, 6, 244-260, 1997.

Kirby, S.H., Rheology of the lithosphere, *Rev. Geophys. Space Phys.*, 21, 1458-1487, 1983.

Kirby, S.H., E.R. Engdahl, and R. Denlinger, Intermediate-depth intraslab earthquakes and arc volcanism as physical expressions of crustal and uppermost mantle metamorphism in subducting slabs, in *Subduction: top to bottom*, edited by G.E. Bebout, D. Scholl, S. Kirby, and J.P. Platt, Am. Geophys. Union, Washington D.C., pp. 195-214, 1996.

Kohlstedt, D.L., and B. Evans, and S.J. Mackwell, Strength of the lithosphere: Constraints imposed by laboratory experiements, *J. Geophys. Res.*, 100, 17587-17602, 1995.

Korgen, B.J., G. Bodvarsson, and R.S. Mesecar, Heat flow through the floor of Cascadia Basin, *J. Geophys. Res.*, 76, 4758-4774, 1971.

Lachenbruch, A.H., Preliminary geothermal model of the Sierra Nevada, *J. Geophys. Res.*, 73, 6977-6989, 1968.

Lachenbruch, A.H., Crustal temperature and heat production - implications of the linear heat-flow relation, *J. Geophys. Res.,*, *75*, 3291-3300, 1970.

Lachenbruch, A.H., and J.H. Sass, Heat flow and energetics of the San Andreas Fault zone, *J. Geophys. Res.*, 76, 6185-6822, 1980.

Langseth, M.G., and E.A. Silver, The Nicoya convergent margin: a region of exceptionally low heat flow, *Geophys. Res. Lett.,* 23, 891–894, 1996.

Lee, Y., D. Deming, and K.F. Chen, Heat flow and heat production in the Arkoma Basin and Oklahoma Platform, southeastern Oklahoma, *J. Geophys. Res.,* 101, 25,387-25,401, 1996.

Lewis, T.J., A.M. Jessop, and A.S. Judge, Heat flux measurements in southwestern British Columbia: the thermal consequences of plate tectonics, *Can. J. Earth Sci.*, 22, 1262-1273, 1985.

Lewis, T.J., W.H. Bentkowski, E.E. Davis, R.D. Hyndman, J.G. Souther, and J.A. Wright, Subduction of the Juan de Fuca Plate; thermal consequences, *J. Geophys. Res.*, *93*, 15207-15225, 1988.

Lyle, M., Koizumi, I., Richter, C., et al., *Proc. ODP, Init. Repts.,* 167: College Station, TX 1997.

MacKay, M.E., G.F. Moore, G.R. Cochrane, J.C. Moore, and L.D. Kulm, Landward vergence and oblique structural trends in the Oregon margin accretionary prism: Implications and effect of fluid flow, *Earth and Planet. Sci. Lett.*, 109, 477-491, 1992.

Mase, C. W., J.H. Sass, A.H. Lachenbruch, R.J. Munroe, Preliminary heat flow investigations of the California Cascades Pagination: 242 Series/Source: Open-File Rep. U. S. Geol. Sur., 1982.

Matsubayashi, O., Y. Okubo, T. Yamazaki, M. Joshima, and T. Miyazaki, Heat-flow and Curie point depth map of Japan and adjoining areas, in *Geological Atlas of Japan,* 2nd ed., sheet 15, Geol. Surv. of Japan, 1992.

McKenna, J.R., Thermal structure in the shallow portion of the Cascadia subduction zone, northern Oregon: implications for décollement strength and earthquake potential, *M.S. Thesis*, Southern Methodist University, pp. 96, 1997.

McNeill, L.C., C. Goldfinger, L.D. Kulm, and R.S. Yeats, Tectonics of the Neogene Cascadia forearc basin: Investigations of a deformed late Miocene unconformity, *Geol. Soc. Am. Bull.*, 112, 1209-1224, 2000.

Molnar, P. and P. England, Temperature, heat flux, and frictional stress near major thrust faults, *J. Geophys. Res., 95, 4833-4856, 1990.*

----------, Temperatures in zones of steady state underthrusting of young oceanic lithosphere, *Earth Palnet. Sci. Lett.*, 131 57-70, 1995.

Moran, J.E., and C.R.B. Lister, Heat flow across Cascadia Basin near 47 °N, 128 °W, *J. Geophys. Res.*, 92, 11416-11432, 1987.

Moore, J.C., K. Moran, M.E. MacKay, H. Tobin, Frontal thrust accretionary prism: geometry, physical properties, and fluid pressures, in *Proceedings of the Ocean Drilling Program, Scientific Results*, vol 146 pt. 1, edited by B. Carson, G.K. Westbrook, R.J. Musgrave, and E. Suess, 359-366, 1995.

Nelson, A.R., and S.F. Personius, Great earthquake potential in Oregon and Washington; an overview of recent coastal geologic studies and their bearing on segmentation of Holocene ruptures, central Cascadia subduction zone, *U. S. Geol. Sur. Prof. Paper 91-114*, 1996.

Oleskevich, D.A., R.D. Hyndman, and K. Wang, The updip and downdip limits to great subduction earthquakes: thermal and structural models of Cascadia, south Alaska, SW Japan, and Chile, *J. Geophys. Res.*, 104, 14965-14991, 1999.

Oppenheimer, D., G. Beroza, G. Carver, and others, The Cape Mendocino, California earthquakes of April 1992: subduction at the triple junction, *Science*, 261, 433-438, 1992.

Pacheco, J.F., L.R. Sykes, and C.H. Scholz, Nature of seismic coupling along simple plate boundaries of the subduction type, *J. Geophys. Res.*, 98, 14133-14159, 1993.

Pardo, M. and G. Suarez, Shape of the subducted Riveria and Cocos plate in southern Mexico: Seismic and tectonic implications, *J. Geophys. Res.*, 100, 12357-12373, 1995.

Parsons, B., and J.G. Sclater, An analysis of the variation of ocean floor bathymetry and heat flow with age, *J. Geophys. Res.*, 82, 803-827, 1977.

Peacock, S.M., The importance of blueschist-eclogite dehydration reactions in subducting oceanic crust, *Geol. Soc. Am. Bull.*, 105, 684-694, 1993.

Peacock, S.M., and R.D. Hyndman, Hydrous minerals in the mantle wedge and the maximum

depth of subduction thrust earthquakes, *Geophys. Res Lett.*, *26*, 2517-2520, 1999.

Peacock, S.M., and K. Wang, Seismic consequences of warm versus cool subduction zone metamorphism: Examples from northeast and southwest Japan, *Scienc*e, *28*6, 937-939, 1999.

Pribnow, D., C.F. Williams, J.H. Sass, and R. Keating, Thermal conductivity of water-saturated rocks from the KTB pilot hole at temperatures of 25 to 300 degrees C, *Geophys. Res. Lett*, 23, 391-394, 1996.

Riddihough, R.P., Recent movements of the Juan de Fuca plate system, *J. Geophys. Res.*, 89, 6980-6994, 1984.

Robertson, E.C., *Thermal Properties of Rocks*, *U.S. Geol. Surv. Open File Rep., 88-441*, 1989.

Rogers, G.C., An assessment of the megathrust earthquake potential of the Cascadia subduction zone, *Can. J. Earth Sci.*, 25, 844-852, 1988.

Roy, R.F., D.D. Blackwell, and F. Birch, Heat generation of plutonic rocks and continental heat flow provinces, *Earth and Planet. Sci. Lett.*, 5, 1-12, 1968.

Roy, R.F., D.D. Blackwell, and E.R. Decker, Continental heat flow, in *The Nature of the Solid Earth,* edited by E.C. Robertson, 506-543, McGraw-Hill, New York, 1972.

Rudnick, R.L., and D.M. Fountain, Nature and composition of the continental crust; a lower crustal perspective, *Rev. Geophys*, 33, 267-309, 1995.

Ruff, L.J., and H. Kanamori, Seismicity and the subduction process, *Phys. Earth Planet. Inter.*, 23, 240-252, 1980.

Rybach, L., Amount and significance of radioactive heat source in sediments, in *Proceedings of the IFP Exploration Research Conference: Thermal Modeling in Sedimentary Basins*, edited by Jean Burrus, 1985.

Satake, K., and Y. Tanioka, Seismogenic and tsunamigenic processes in shallow subduction zones, *Pure and Appl. Geophys.*, 154, 467-483, 1999.

Savage, J.C., M. Lisowski, M., and W.H. Prescott, Strain accumulation in western Washington, *J. Geophys. Res.*,96, 14493-14507, 1991.

Scholz, C.H., *The Mechanics of Earthquakes and Faulting*, 439 pp., Cambridge University Press, New York, 1990.

Sibson, R.H., Continental fault structure and the shallow earthquake source, *J. Geol. Soc. London*, 140, 741-767, 1983.

Silver, E.A., Synthesis of fluid-structural relationships of the Pacific margin of Costa Rica, in

Ocean Drilling Program, Sci. Results, 170, edited by E.A. Silver, G. Kimura, and T.H. Shipley, 1–11 [CD-ROM], Ocean Drilling Program, College Station, Texas, 2001.

Smith, S.W., J.S. Knapp, and R.C. McPherson, Seismicity of the Gorda plate, structure of the continental margin, and an eastward jump of the Mendocino Triple Junction, *J. Geophys. Res.*, 98, 8153-8171, 1993.

Snavely, P.D., Geologic cross section across the continental margin off Cape Flattery, Washington , and Vancouver Island, British Columbia, *U.S. Geol. Surv. Open File Rep., 81-0978*, 1981.

Snavely, P.D., H.C. Wagner, W.W. Rau, and D. Bukry, Correlation of Tertiary rocks penetrated in wells drilled on the southern Oregon continental margin, *U.S. Geol. Surv. Open File Rep., 81-1351*, 1981.

Snay, R.A., and T. Matsikari, Horizontal deformation in the Cascadia subduction zone as derived from serendipitous geodetic data, *Tectonophysics*, 194, 59-67, 1991.

Springer, M, and A. Forster, Heat-flow density across the Central Andean subduction zone, *Tectonophysic*s, 291, 123-139, 1998.

Stein, S., J.F. Engeln, D.A. Wiens, R.C. Speed, and K. Fujita, Slow subduction of old lithosphere in the Lesser Antilles, *Tectonophysics*, 99, 139-148, 1983.

Suarez, G., T. Monfret, G. Wittlinger, and Christian David, Geometry of subduction and depth of the seismogenic zone in the Guerrero gap, Mexico, *Nature*, 345, 336-338, 1990.

Tichelaar, B.W., and L.J. Ruff, Depth of seismic coupling along subduction zones, *J. Geophys. Res.*, 98, 2017-2037, 1993.

Tréhu, A. M., I. Asudeh, T.M. Brocher, J.H. Luetgert, W.D. Mooney, J.L. Nabelek, Y. Nakamura, Crustal architecture of the Cascadia forearc, *Science*, 266, 237-243, 1994.

Tréhu, A. M., G. Lin, E. Maxwell, and C. Goldfinger, A Seismic reflection profile across the Cascadia subduction zone offshore Oregon: New constraints on methane distribution and crustal structure, *J. Geophys. Res.*, 100, 15101-15116, 1995.

Turcotte, D.L., and G. Schubert, Geodynamics: *Applications of continuum physics to geological problems*, John Wiley, New York, pp. 450, 1982.

Verdonck, D., and G. Zandt, Three-dimensional crustal structure of the Mendocino Triple Junction region from local earthquake travel times, *J. Geophys. Res.*, 99, 23843-23858, 1994.

von Herzen, R., C. Ruppel, P. Molnar, M. Nettles, S. Nagihara, and G. Ekstrom; A constraint on the shear stress at the Pacific-Australian Plate at the Kermadec forearc, *J. Geophys. Res.*, 106, 6817-6833, 2001.

von Huene, R. and L .Homa, The possible effect of pore-fluid pressure in subduction zones, in *Studies in Continental Margin Geology*, *AAPG Mem*., 34, edited by J.S. Watkins and C.L. Drake, pp.781-791, 1982.

Wang, K., T. Mulder, G.C. Rogers, and R.D. Hyndman, Case for very low coupling stress on the Cascadia subduction fault, *J. Geophys. Res.*, 100, 12907-12918, 1995a.

Wang, K., R.D. Hyndman, and M. Yamano, Thermal regime of the Southwest Japan subduction zone of age history of the subducting plate, *Tectonophysics,* 248, 1995b.

Westbrook, G.K., Carson, B., Musgrave, R.J., et al., *Proc. ODP, Init Repts,*146 (Pt. 1), College Station, Texas, 1994.

Wollenberg, H.A., and A.R. Smith, Radiogenic heat production of crustal rocks: An assesment based on geochemical data, *Geophys. Res. Lett.*, 14, 295-298, 1987.

Ziagos, J.P., D.D. Blackwell, and F. Mooser, Heat flow in southern Mexico and the thermal effects of subduction, *J. Geophys. Res.*, 90, 5410-5420, 1985.

Figure 1

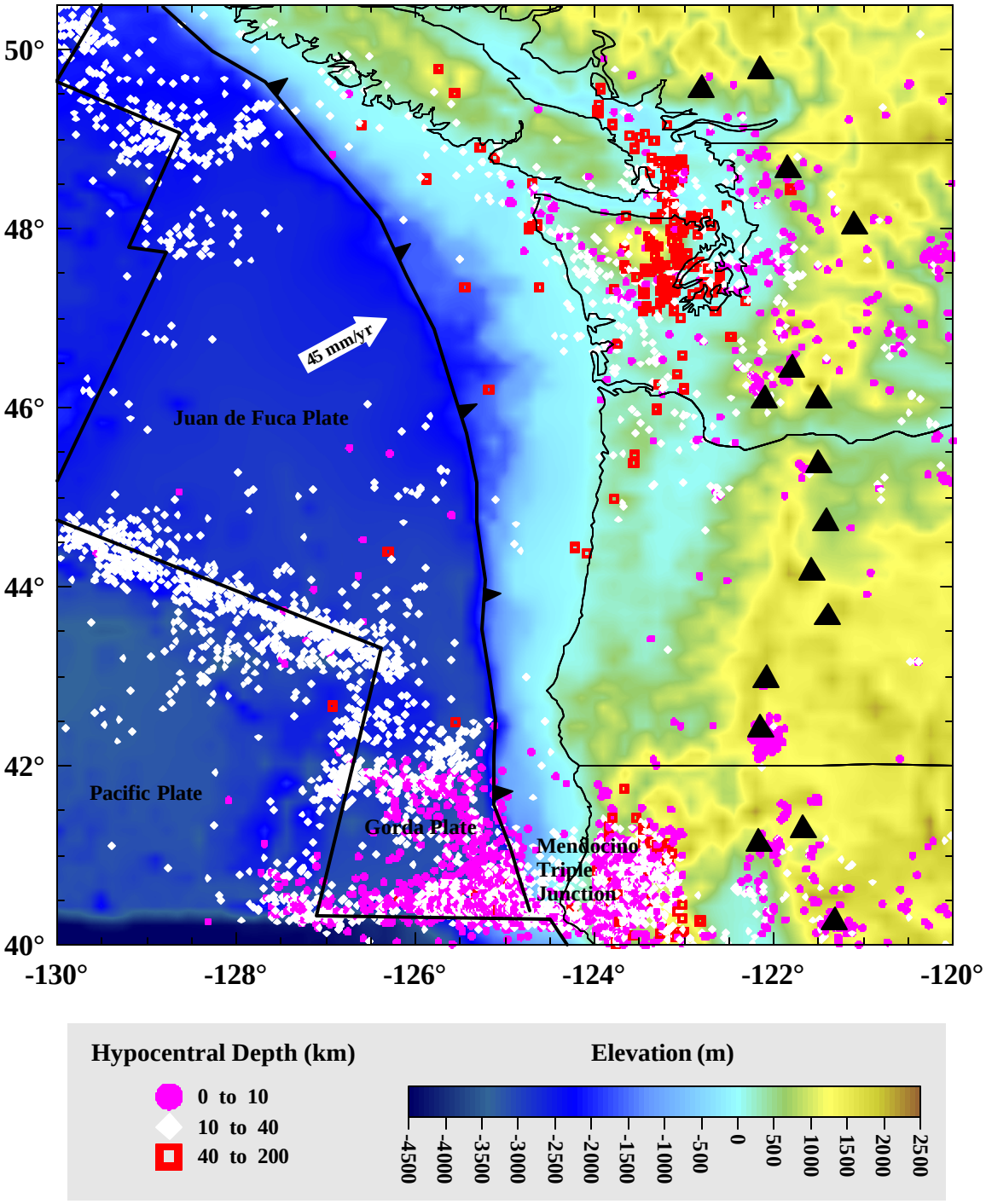
50°
48°
46°
44°
42°
40°
-130°
-128°
-126°
-124°
-122°
-120°
45 mm/yr
Juan de Fuca Plate
Pacific Plate
Gorda Plate
Mendocino
Triple
Junction
Hypocentral Depth (km)
0 to 10
10 to 40
40 to 200
Elevation (m)
-4500
-4000
-3500
-3000
-2500
-2000
-1500
-1000
-500
0
500
1000
1500
2000
2500

Figure2

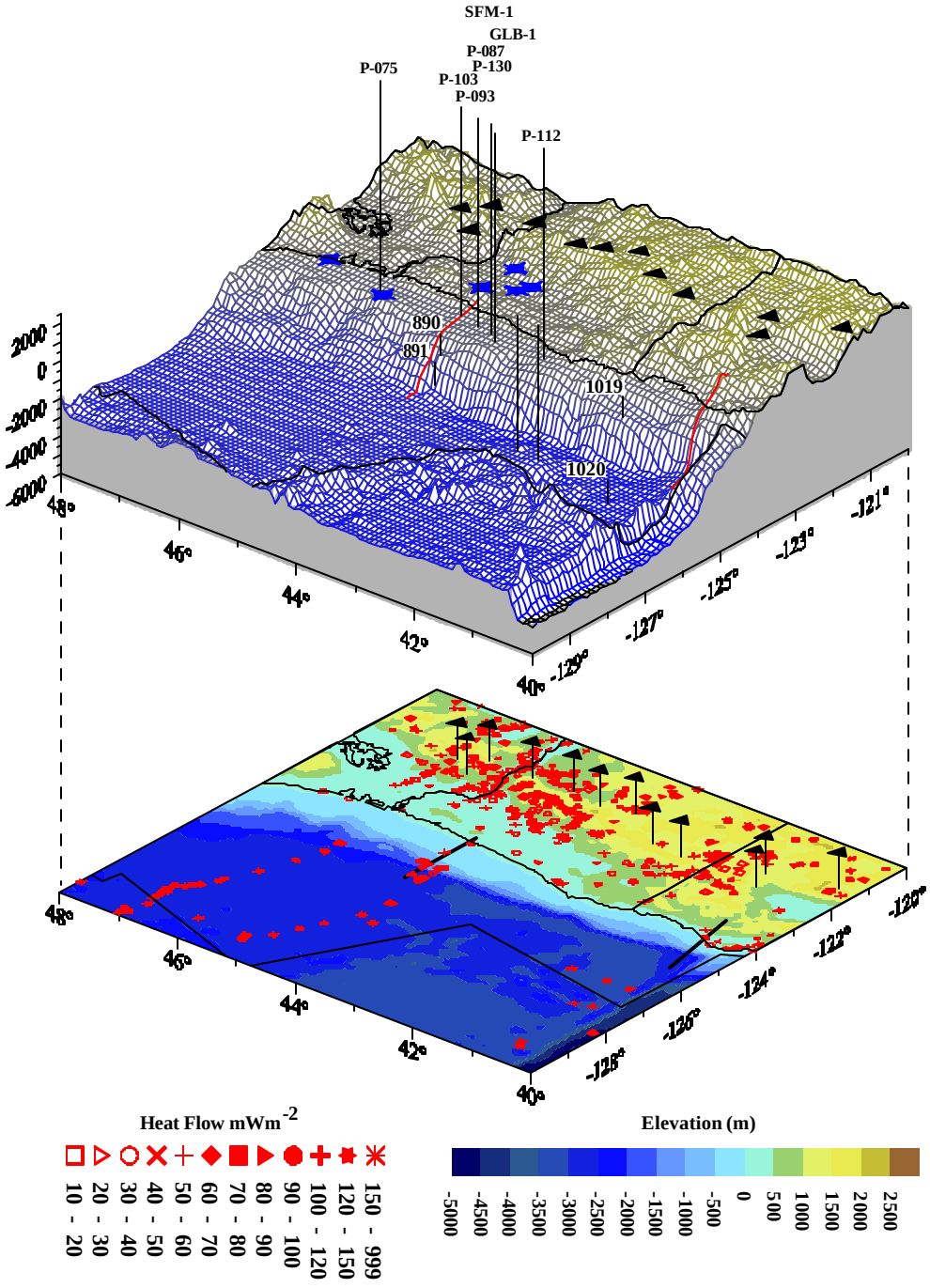
SFM-1
GLB-1
P-087
P-130
P-103
P-093
P-075
P-112
890
891
1019
1020
2000
0
-2000
-4000
-6000
48°
46°
44°
42°
40°
-120°
-121°
-123°
-125°
-127°
-122°
-124°
-126°
-128°
Heat Flow mWm-2
10 - 20
20 - 30
30 - 40
40 - 50
50 - 60
60 - 70
70 - 80
80 - 90
90 - 100
100 - 120
120 - 150
150 - 999
Elevation (m)
-5000
-4500
-4000
-3500
-3000
-2500
-2000
-1500
-1000
-500
0
500
1000
1500
2000
2500

Figure 3a

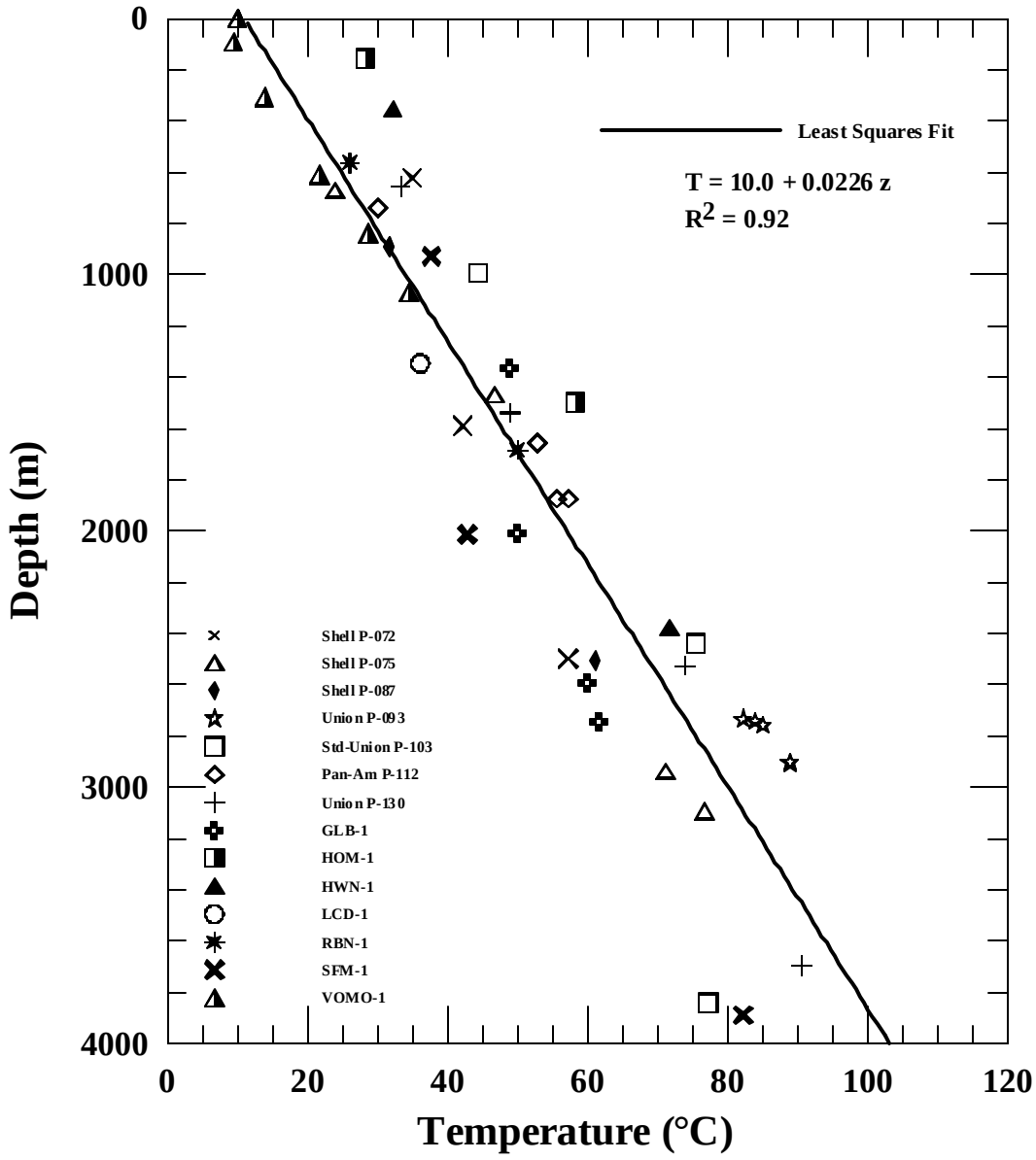
Depth (m)
0
1000
2000
3000
4000
0
20
40
60
80
100
120
Temperature (°C)
Least Squares Fit
T = 10.0 + 0.0226 z
R2 = 0.92
Shell P-072
Shell P-075
Shell P-087
Union P-093
Std-Union P-103
Pan-Am P-112
Union P-130
GLB-1
HOM-1
HWN-1
LCD-1
RBN-1
SFM-1
VOMO-1

Figure 3b

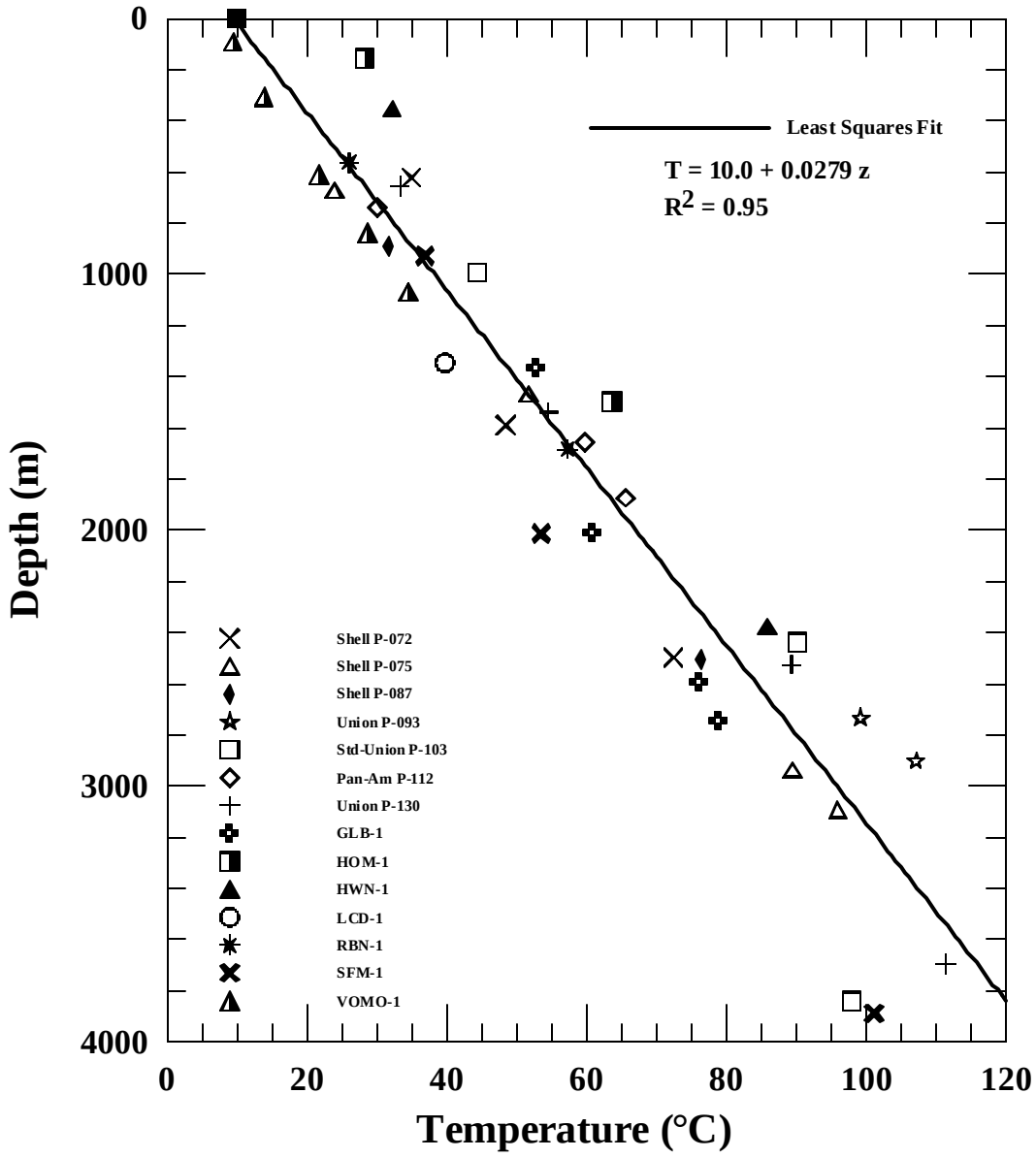
Least Squares Fit
T = 10.0 + 0.0279 z
R2 = 0.95
Shell P-072
Shell P-075
Shell P-087
Union P-093
Std-Union P-103
Pan-Am P-112
Union P-130
GLB-1
HOM-1
HWN-1
LCD-1
RBN-1
SFM-1
VOMO-1
Depth (m)
0
1000
2000
3000
4000
0
20
40
60
80
100
120
Temperature (°C)

Figure 4a

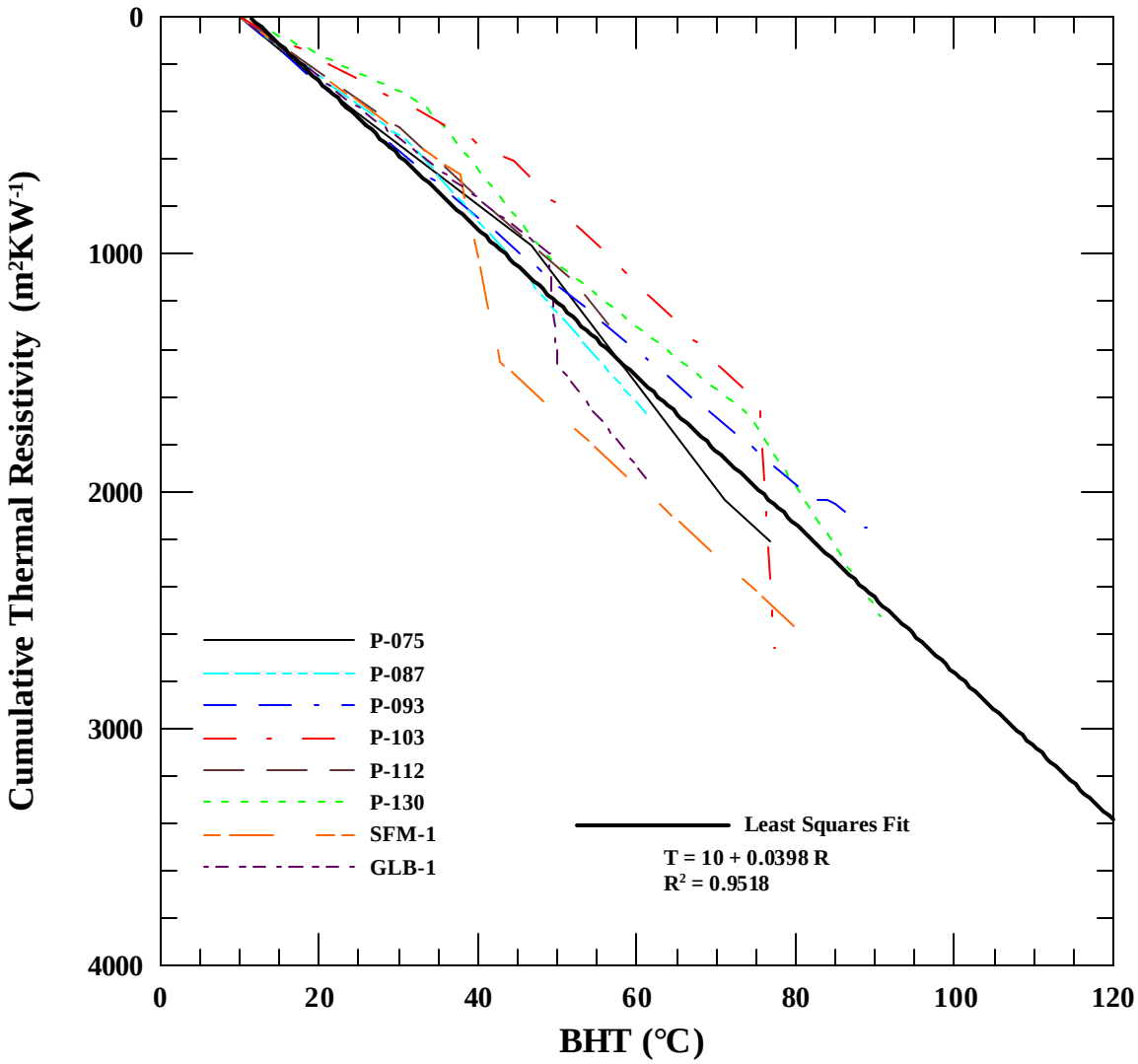
Cumulative Thermal Resistivity (m²KW⁻¹)
0
1000
2000
3000
4000
0
20
40
60
80
100
120
BHT (°C)
P-075
P-087
P-093
P-103
P-112
P-130
SFM-1
GLB-1
Least Squares Fit
T = 10 + 0.0398 R
R² = 0.9518

Figure 4b

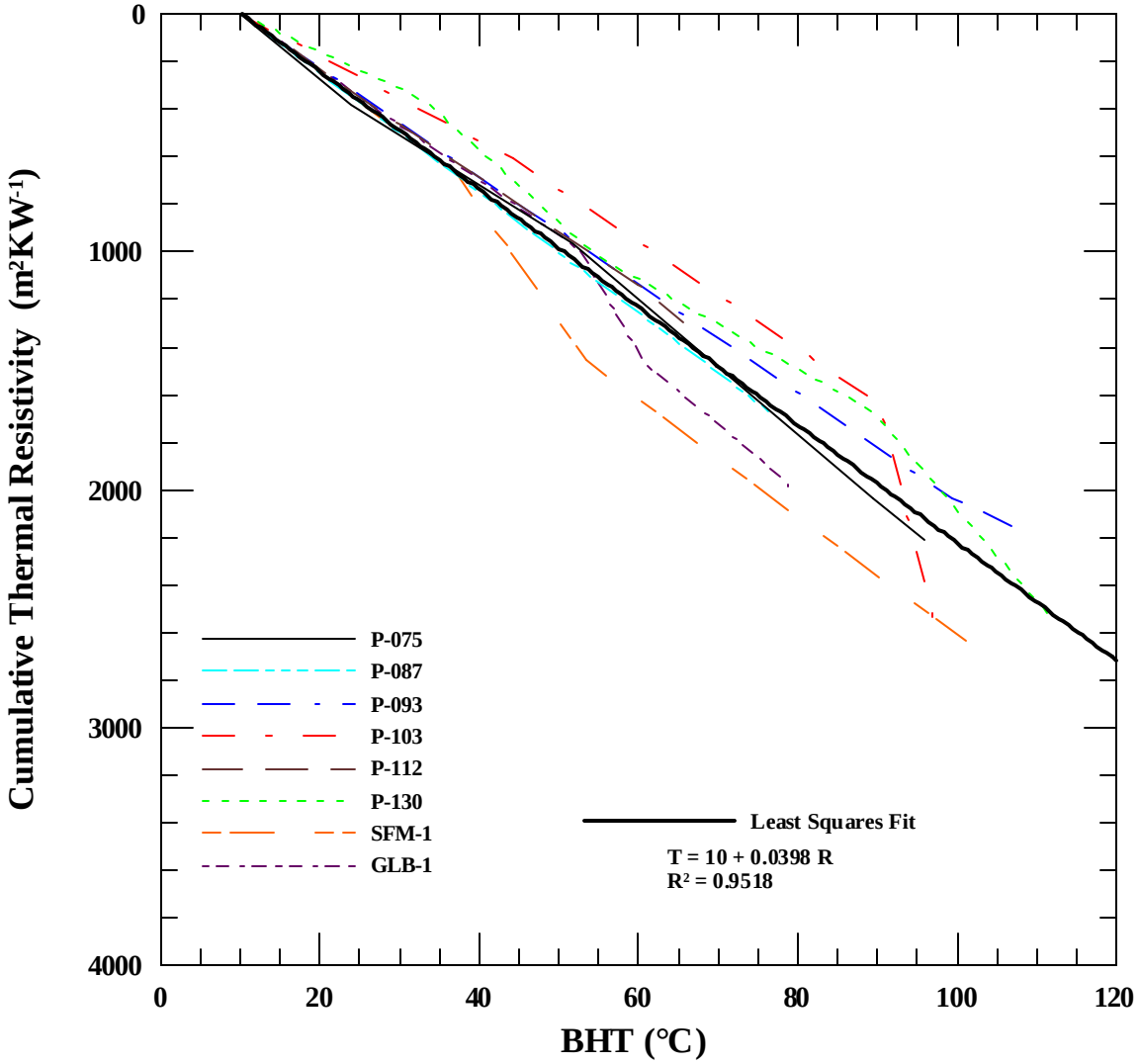
Cumulative Thermal Resistivity (m²KW⁻¹)
0
1000
2000
3000
4000
0
20
40
60
80
100
120
BHT (°C)
P-075
P-087
P-093
P-103
P-112
P-130
SFM-1
GLB-1
Least Squares Fit
T = 10 + 0.0398 R
R² = 0.9518

Figure 5

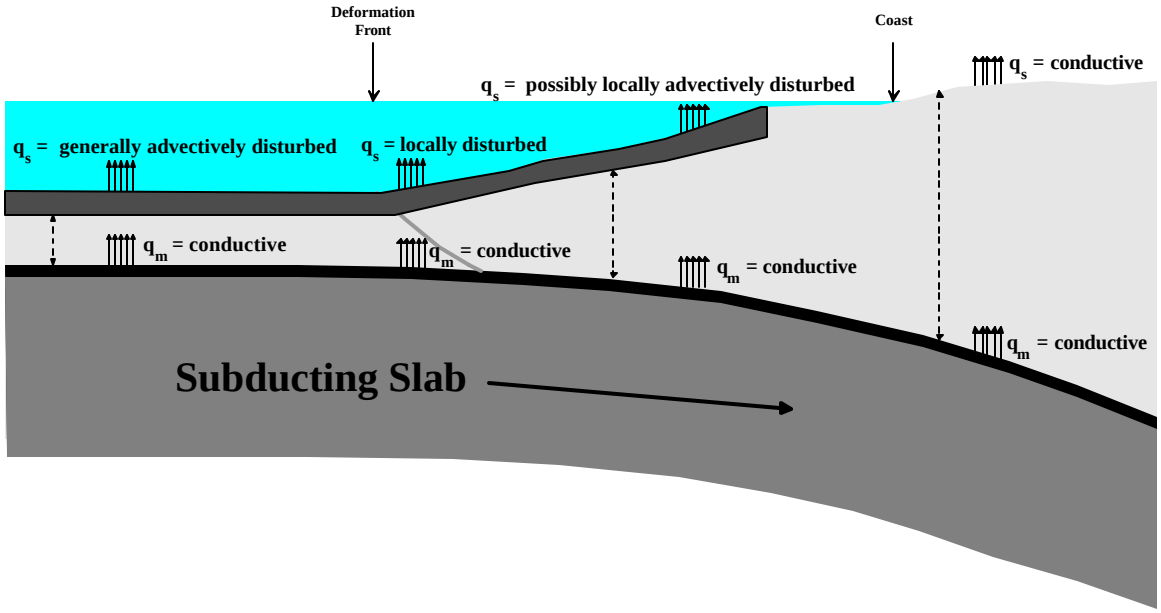
Deformation Front
Coast
q_s = possibly locally advectively disturbed
q_s = conductive
q_s = generally advectively disturbed
q_s = locally disturbed
q_m = conductive
q_m = conductive
q_m = conductive
q_m = conductive
Subducting Slab

Figure 6a

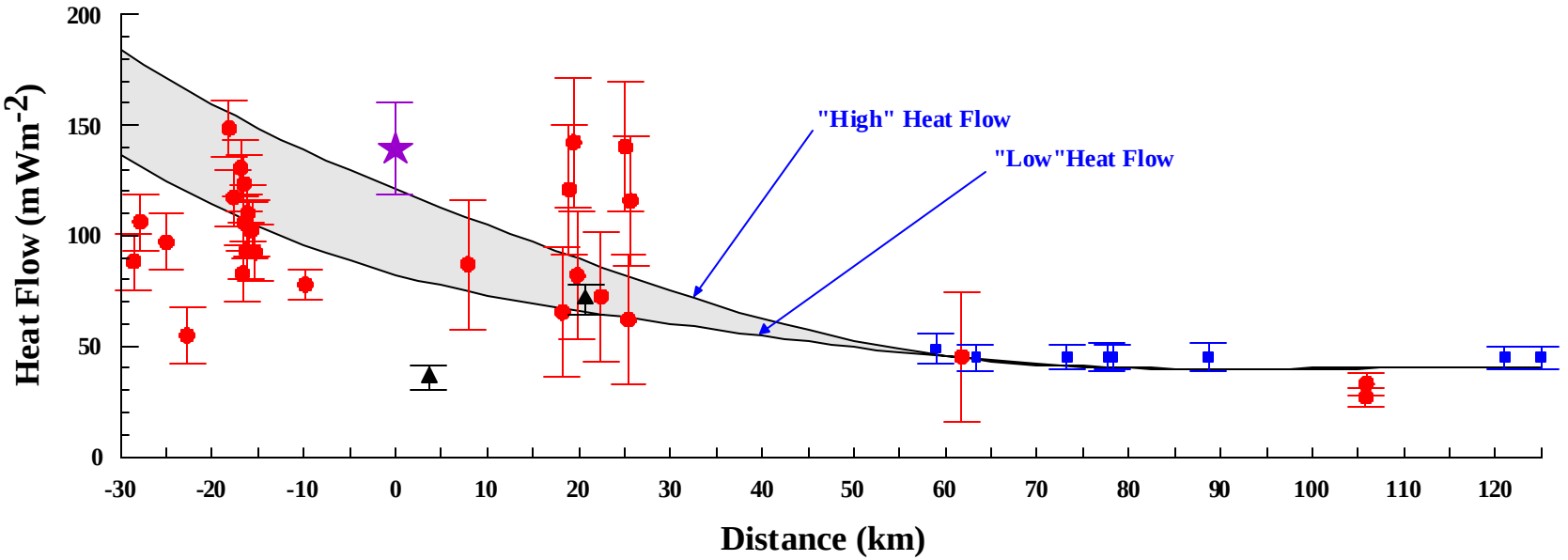
Heat Flow (mWm-2)
200
150
100
50
0
-30
-20
-10
0
10
20
30
40
50
60
70
80
90
100
110
120
Distance (km)
"High" Heat Flow
"Low"Heat Flow

Figure 6b

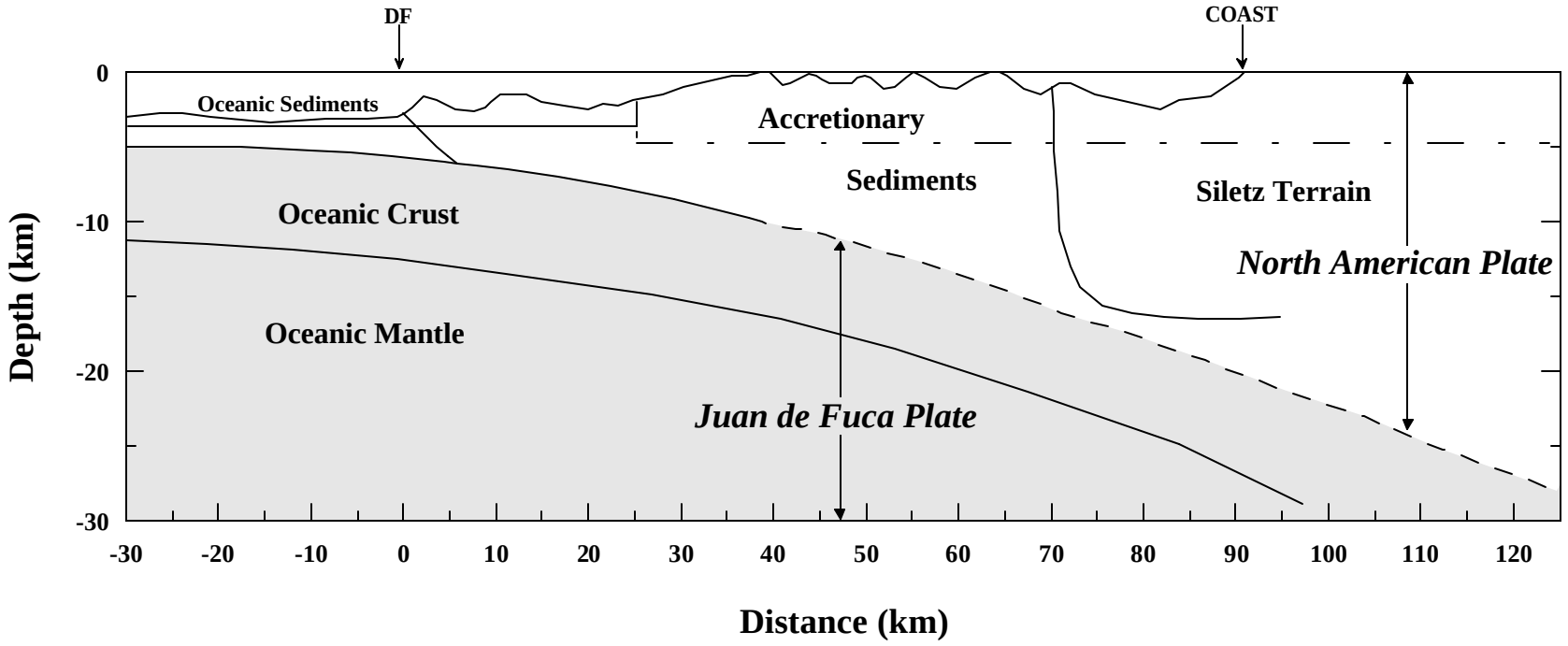
DF
COAST
0
-10
-20
-30
Depth (km)
Oceanic Sediments
Accretionary
Sediments
Siletz Terrain
Oceanic Crust
North American Plate
Oceanic Mantle
Juan de Fuca Plate
-30
-20
-10
0
10
20
30
40
50
60
70
80
90
100
110
120
Distance (km)

Figure 7a

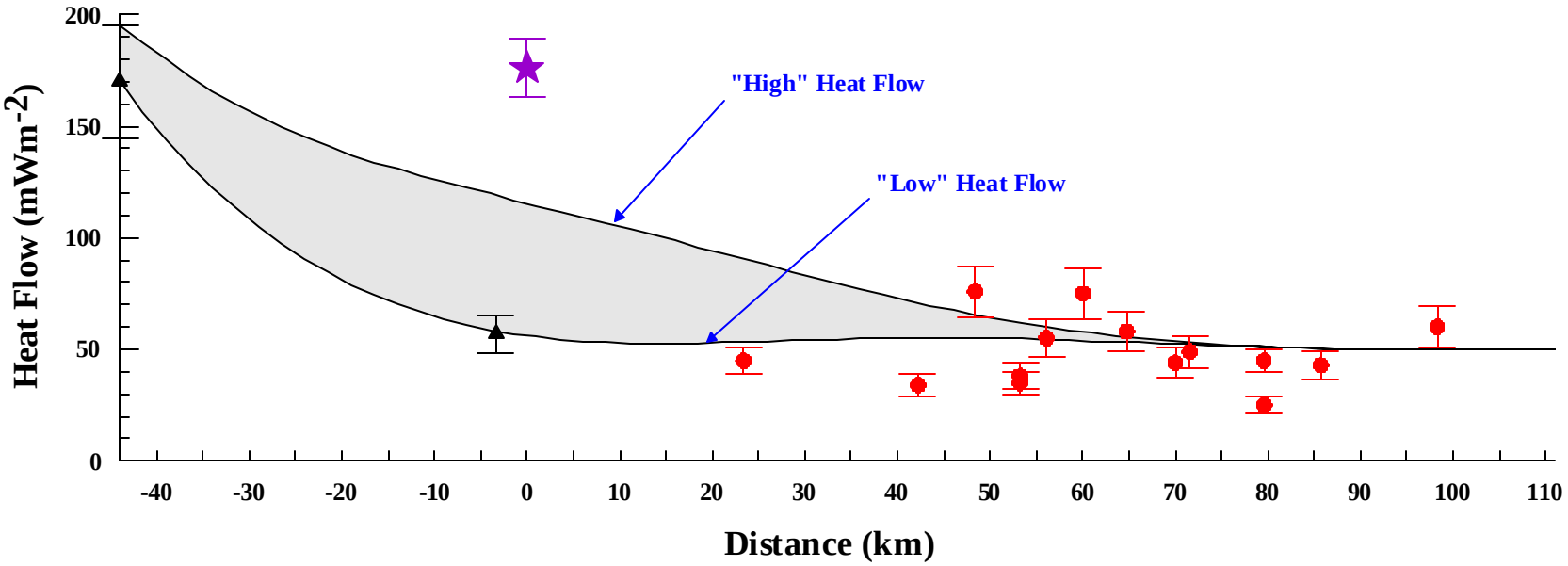
Heat Flow (mWm-2)
200
150
100
50
0
"High" Heat Flow
"Low" Heat Flow
-40
-30
-20
-10
0
10
20
30
40
50
60
70
80
90
100
110
Distance (km)

Figure 7b

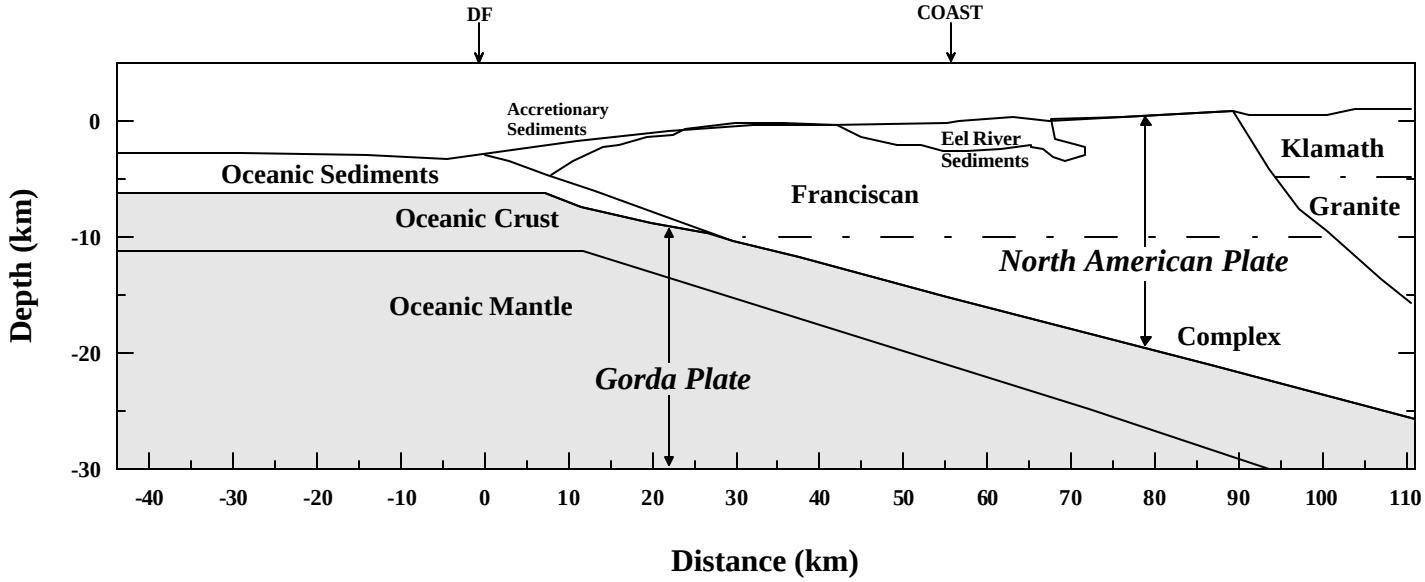
DF
COAST
Accretionary Sediments
Eel River Sediments
Klamath
Granite
Oceanic Sediments
Franciscan
Oceanic Crust
North American Plate
Oceanic Mantle
Complex
Gorda Plate
Depth (km)
0
-10
-20
-30
-40
-30
-20
-10
0
10
20
30
40
50
60
70
80
90
100
110
Distance (km)

Figure 8a

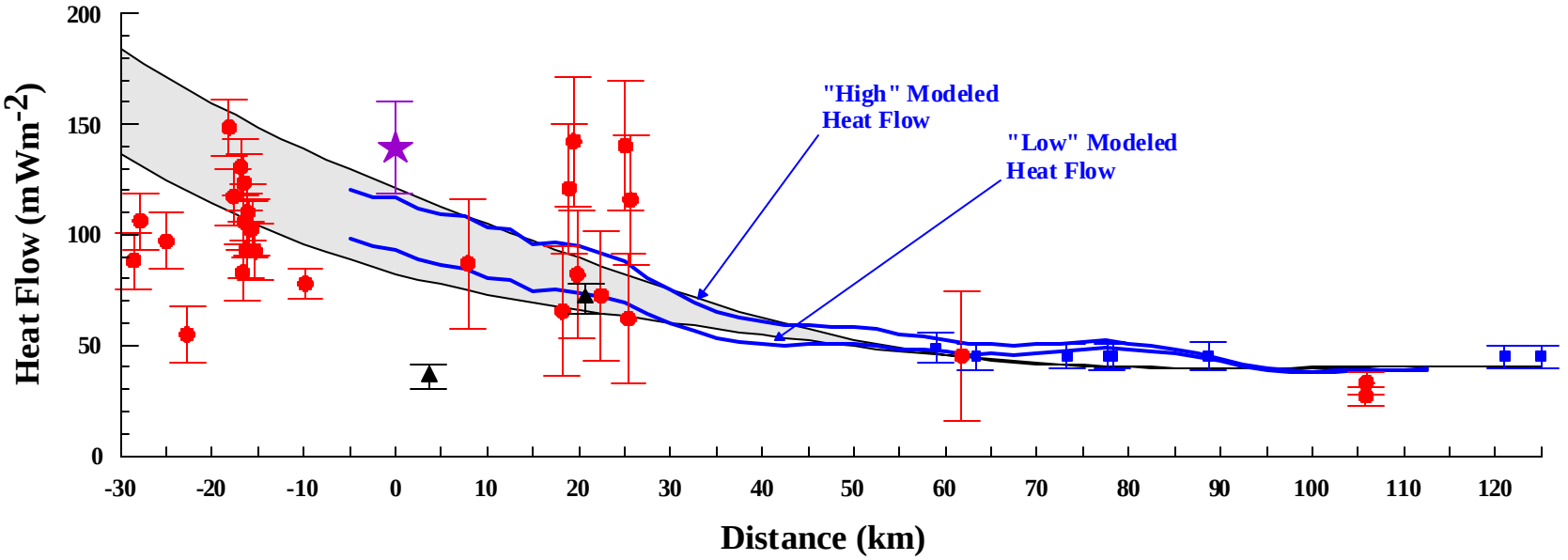
Heat Flow (mWm-2)
200
150
100
50
0
-30
-20
-10
0
10
20
30
40
50
60
70
80
90
100
110
120
Distance (km)
"High" Modeled
Heat Flow
"Low" Modeled
Heat Flow

Figure 8b

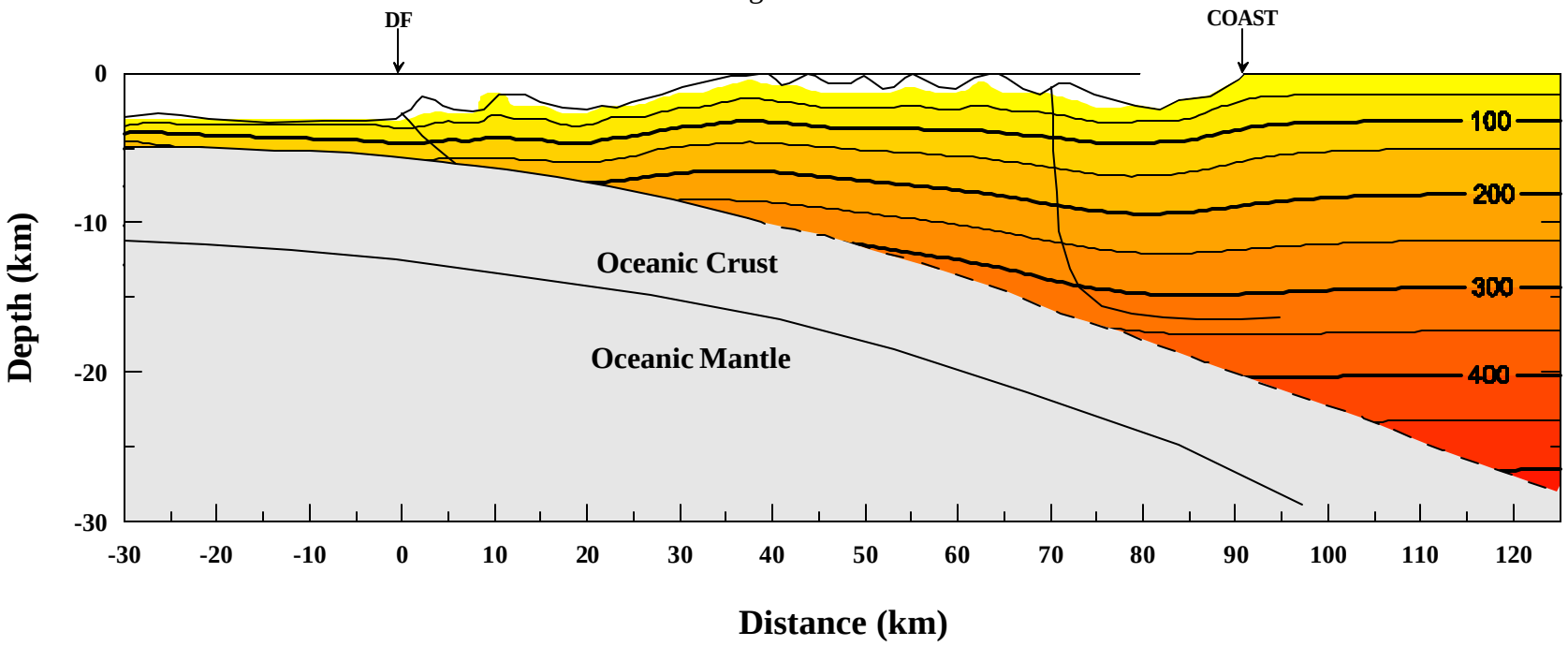
DF
COAST
0
-10
-20
-30
Depth (km)
100
200
300
400
Oceanic Crust
Oceanic Mantle
-30
-20
-10
0
10
20
30
40
50
60
70
80
90
100
110
120
Distance (km)

Figure 8c

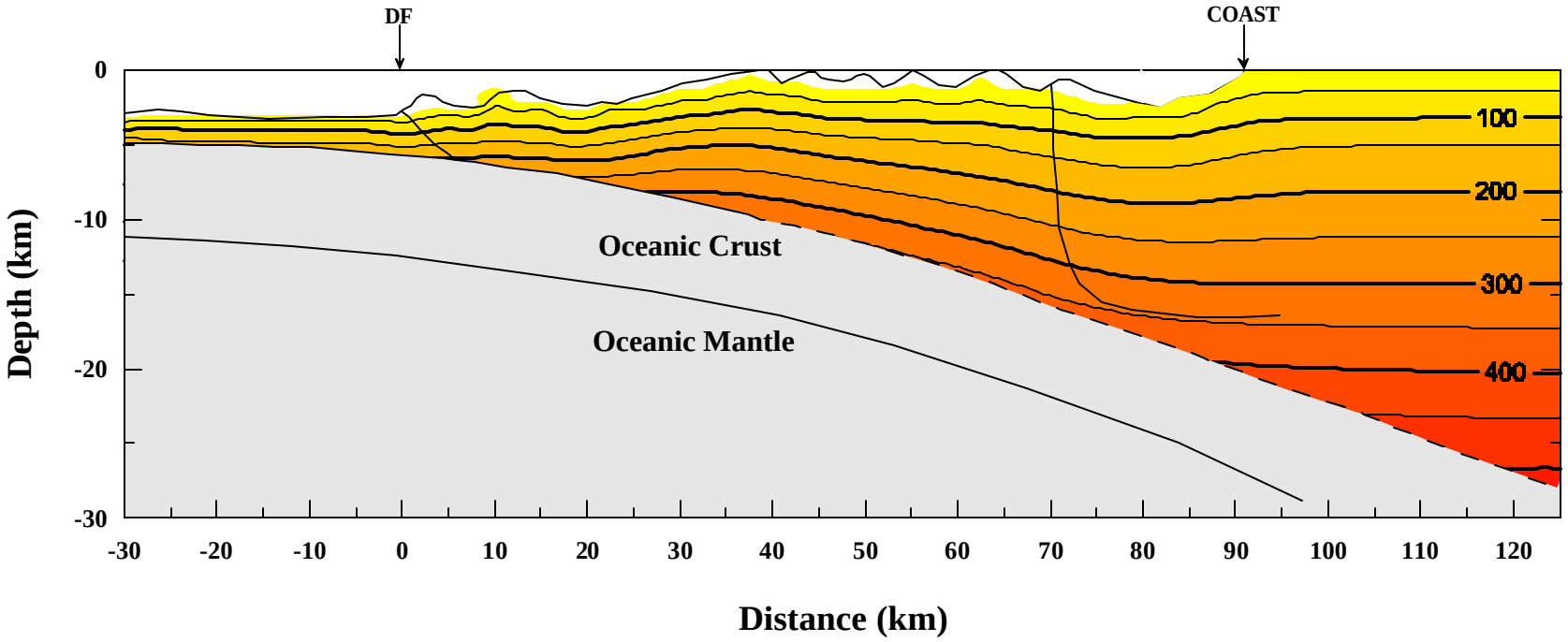
DF
COAST
0
-10
-20
-30
Depth (km)
100
200
300
400
Oceanic Crust
Oceanic Mantle
-30
-20
-10
0
10
20
30
40
50
60
70
80
90
100
110
120
Distance (km)

Figure 9a

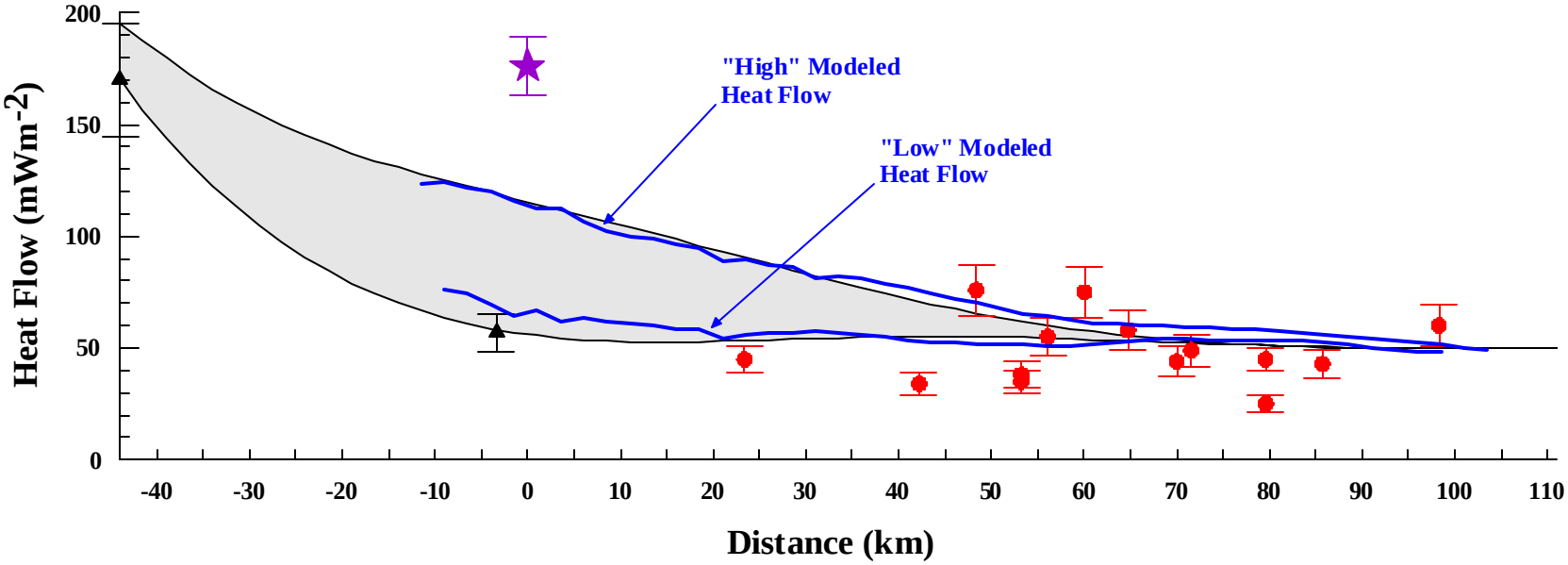
"High" Modeled
Heat Flow
"Low" Modeled
Heat Flow
Heat Flow (mWm-2)
Distance (km)
200
150
100
50
0
-40
-30
-20
-10
0
10
20
30
40
50
60
70
80
90
100
110

Figure 9b

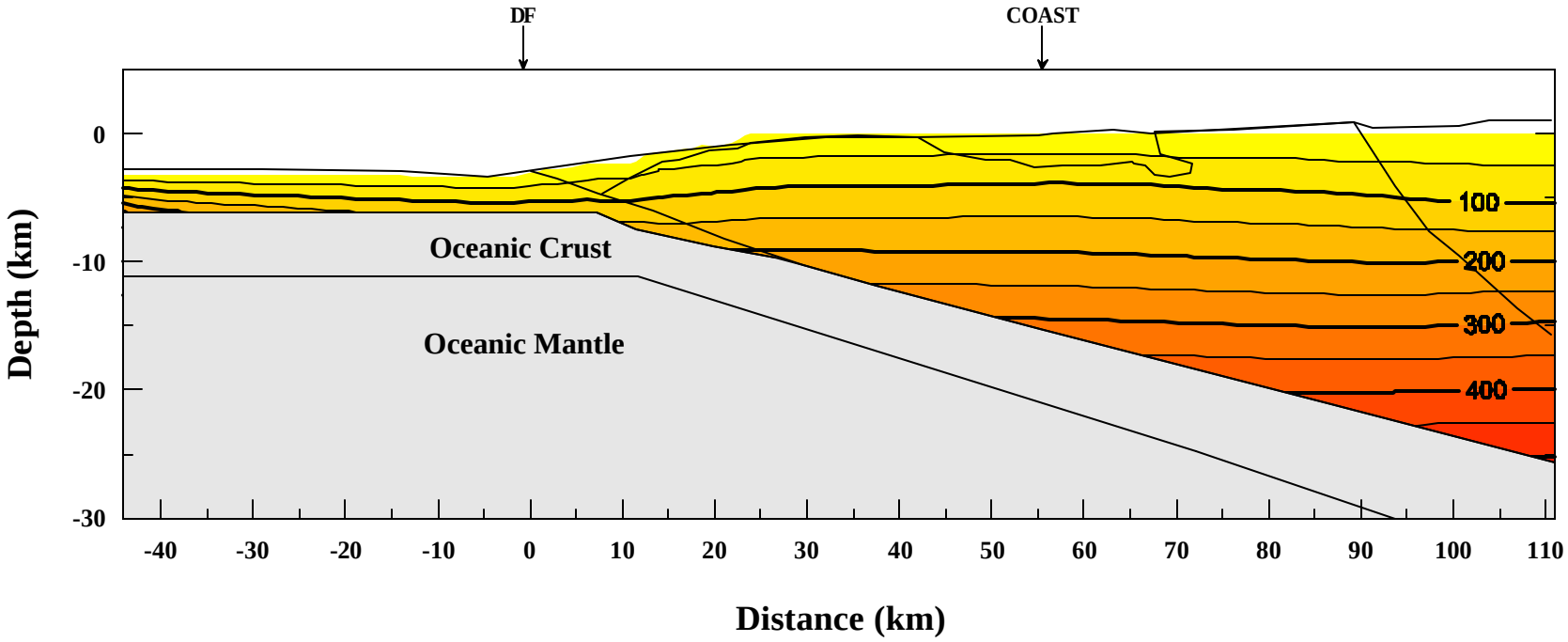
DF
COAST
0
-10
-20
-30
Depth (km)
Oceanic Crust
Oceanic Mantle
100
200
300
400
-40
-30
-20
-10
0
10
20
30
40
50
60
70
80
90
100
110
Distance (km)

Figure 9c

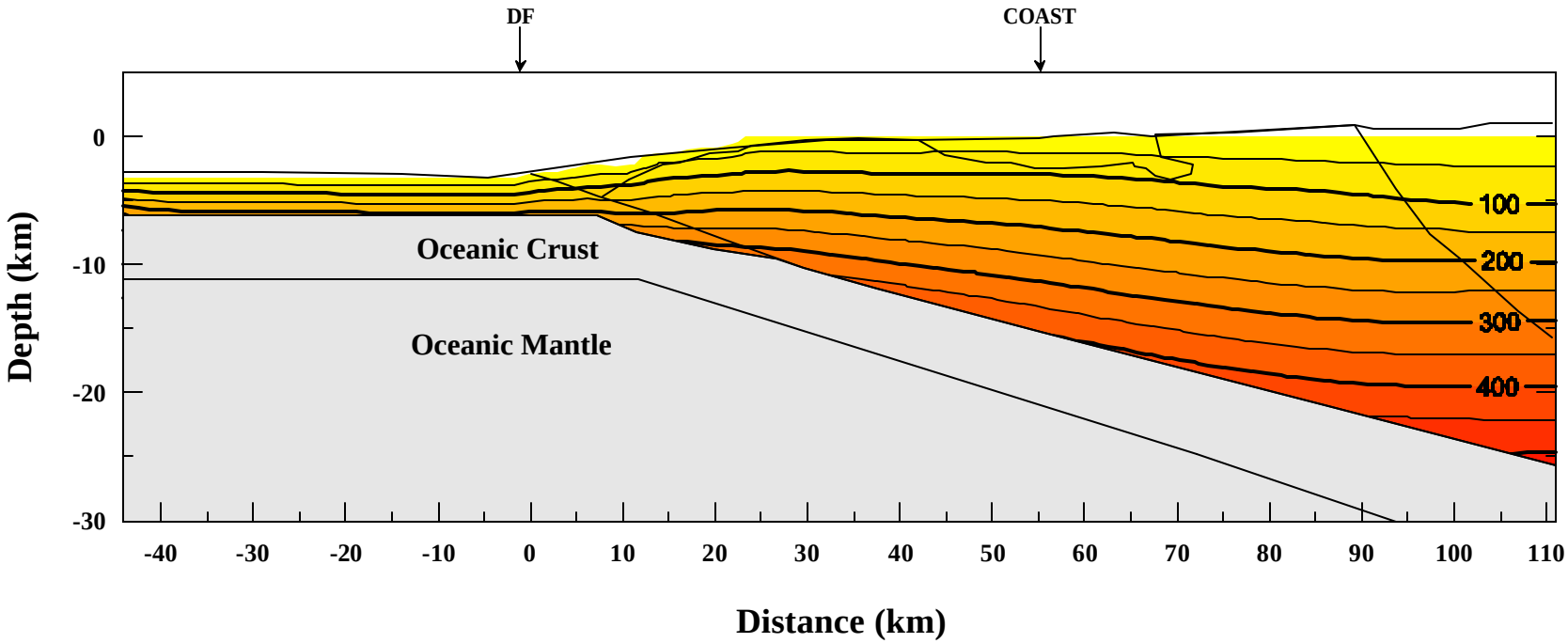
DF
COAST
0
-10
-20
-30
Depth (km)
Oceanic Crust
Oceanic Mantle
100
200
300
400
-40
-30
-20
-10
0
10
20
30
40
50
60
70
80
90
100
110
Distance (km)

Figure 10a

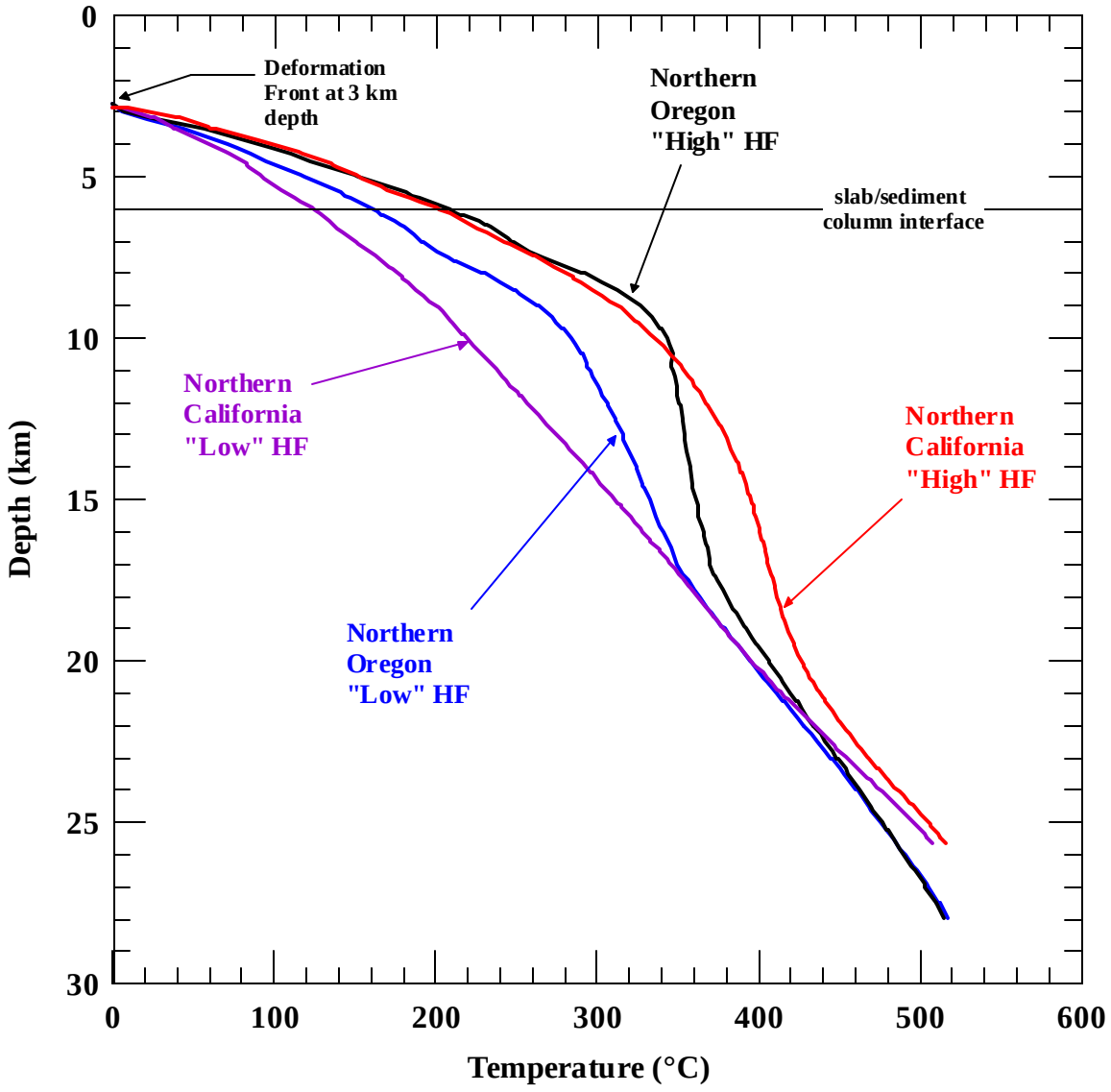
Deformation Front at 3 km depth
Northern Oregon "High" HF
slab/sediment column interface
Northern California "Low" HF
Northern California "High" HF
Northern Oregon "Low" HF
Depth (km)
Temperature (°C)
0
5
10
15
20
25
30
0
100
200
300
400
500
600

Figure 10b

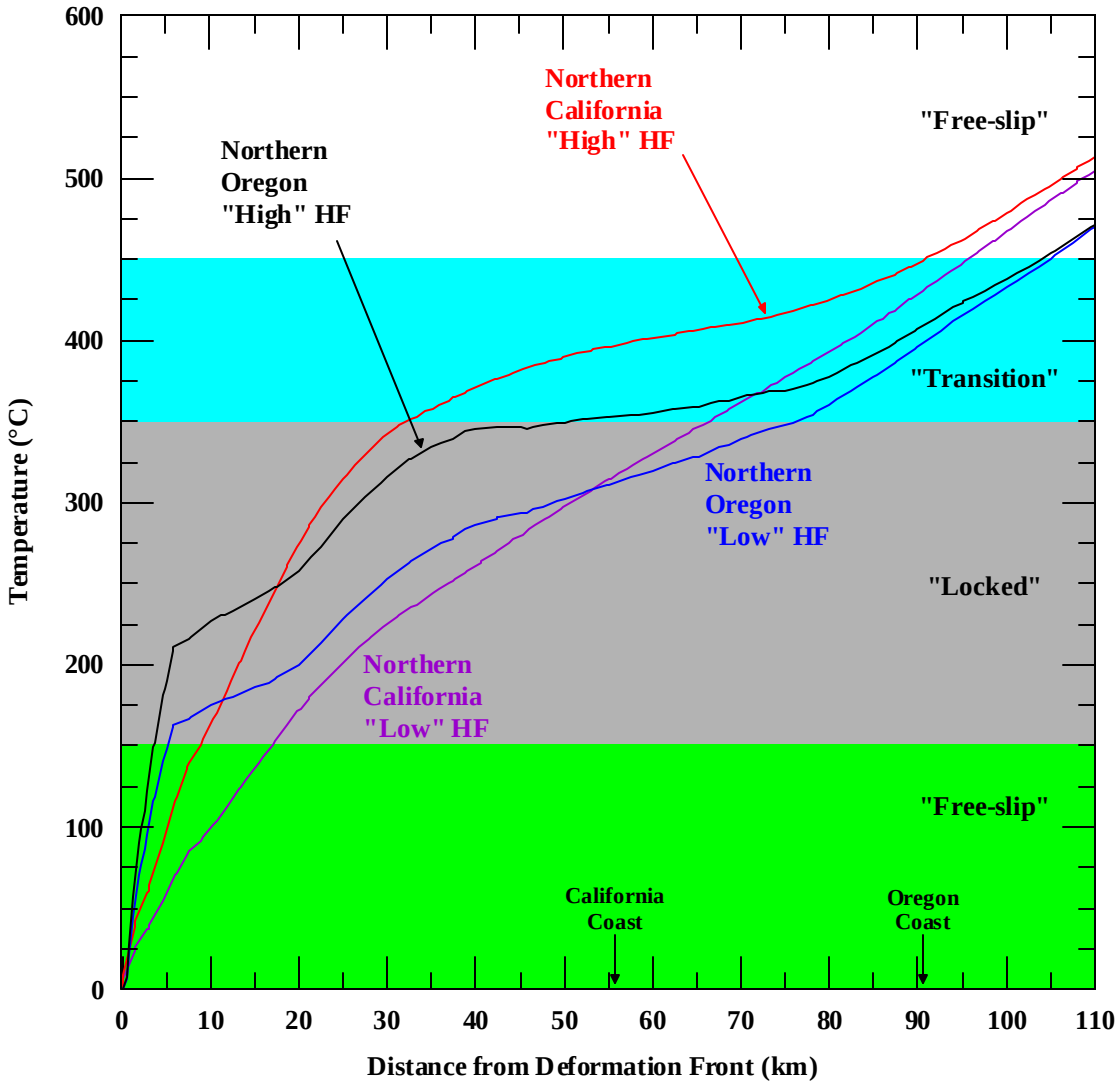
Temperature (°C)
600
500
400
300
200
100
0
0
10
20
30
40
50
60
70
80
90
100
110
Distance from Deformation Front (km)
Northern
California
"High" HF
Northern
Oregon
"High" HF
"Free-slip"
"Transition"
Northern
Oregon
"Low" HF
"Locked"
Northern
California
"Low" HF
"Free-slip"
California
Coast
Oregon
Coast

Figure 11

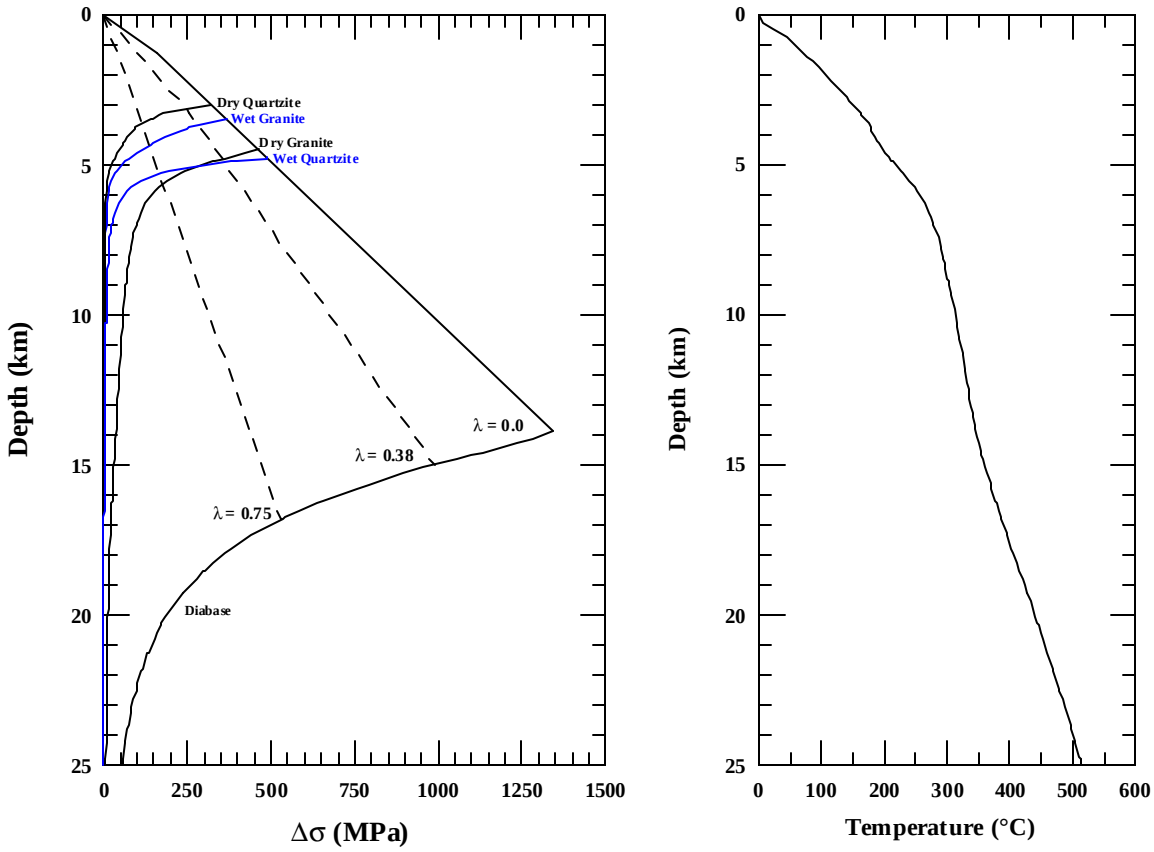
Depth (km)
0
5
10
15
20
25
Dry Quartzite
Wet Granite
Dry Granite
Wet Quartzite
λ = 0.0
λ = 0.38
λ = 0.75
Diabase
0
250
500
750
1000
1250
1500
Δσ (MPa)
Depth (km)
0
5
10
15
20
25
0
100
200
300
400
500
600
Temperature (°C)

Figure 12

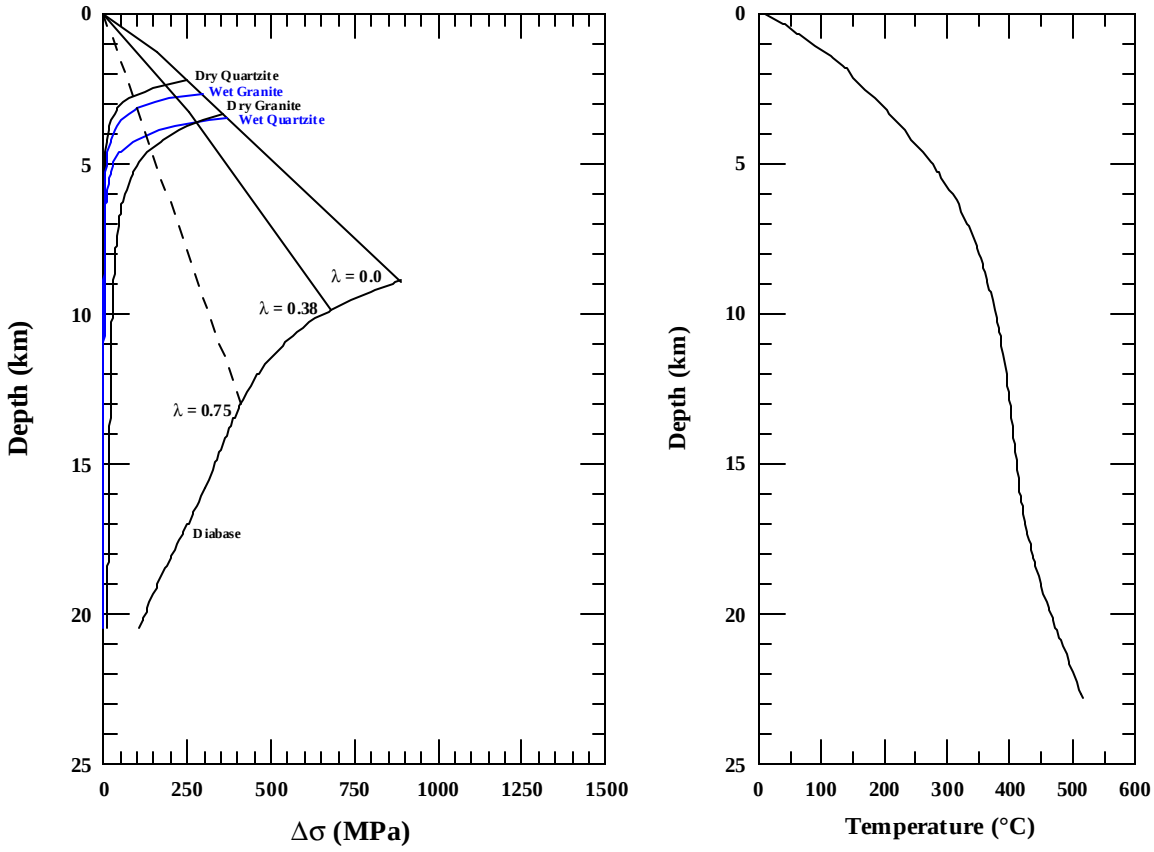
Depth (km)
0
5
10
15
20
25
0
250
500
750
1000
1250
1500
Δσ (MPa)
Dry Quartzite
Wet Granite
Dry Granite
Wet Quartzite
λ = 0.0
λ = 0.38
λ = 0.75
Diabase
Depth (km)
0
5
10
15
20
25
0
100
200
300
400
500
600
Temperature (°C)

Figure 13

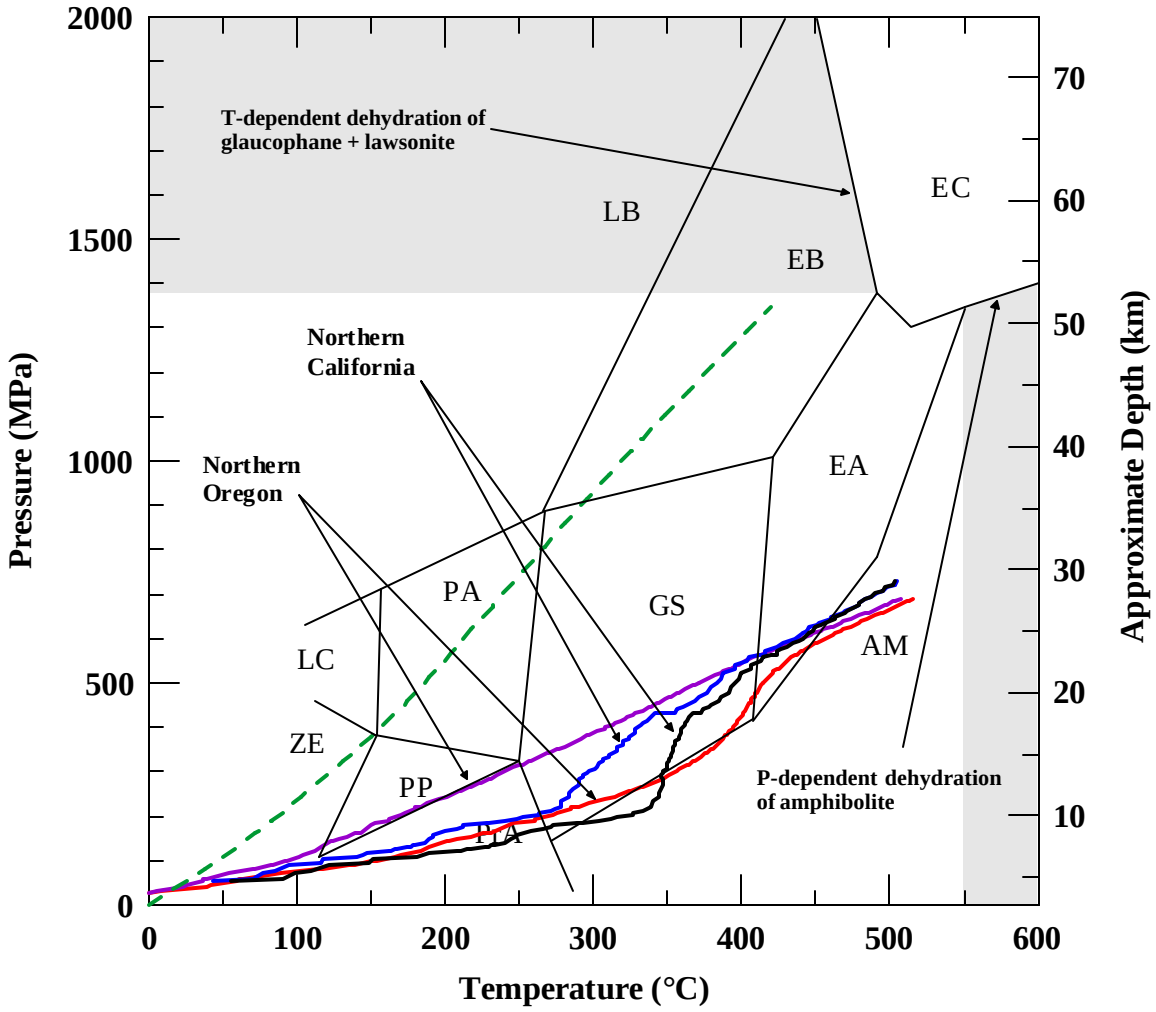
2000
1500
1000
500
0
Pressure (MPa)
0
100
200
300
400
500
600
Temperature (°C)
70
60
50
40
30
20
10
Approximate Depth (km)
T-dependent dehydration of glaucophane + lawsonite
LB
EB
EC
EA
Northern California
Northern Oregon
PA
GS
AM
LC
ZE
PP
PA
P-dependent dehydration of amphibolite

Figure 14

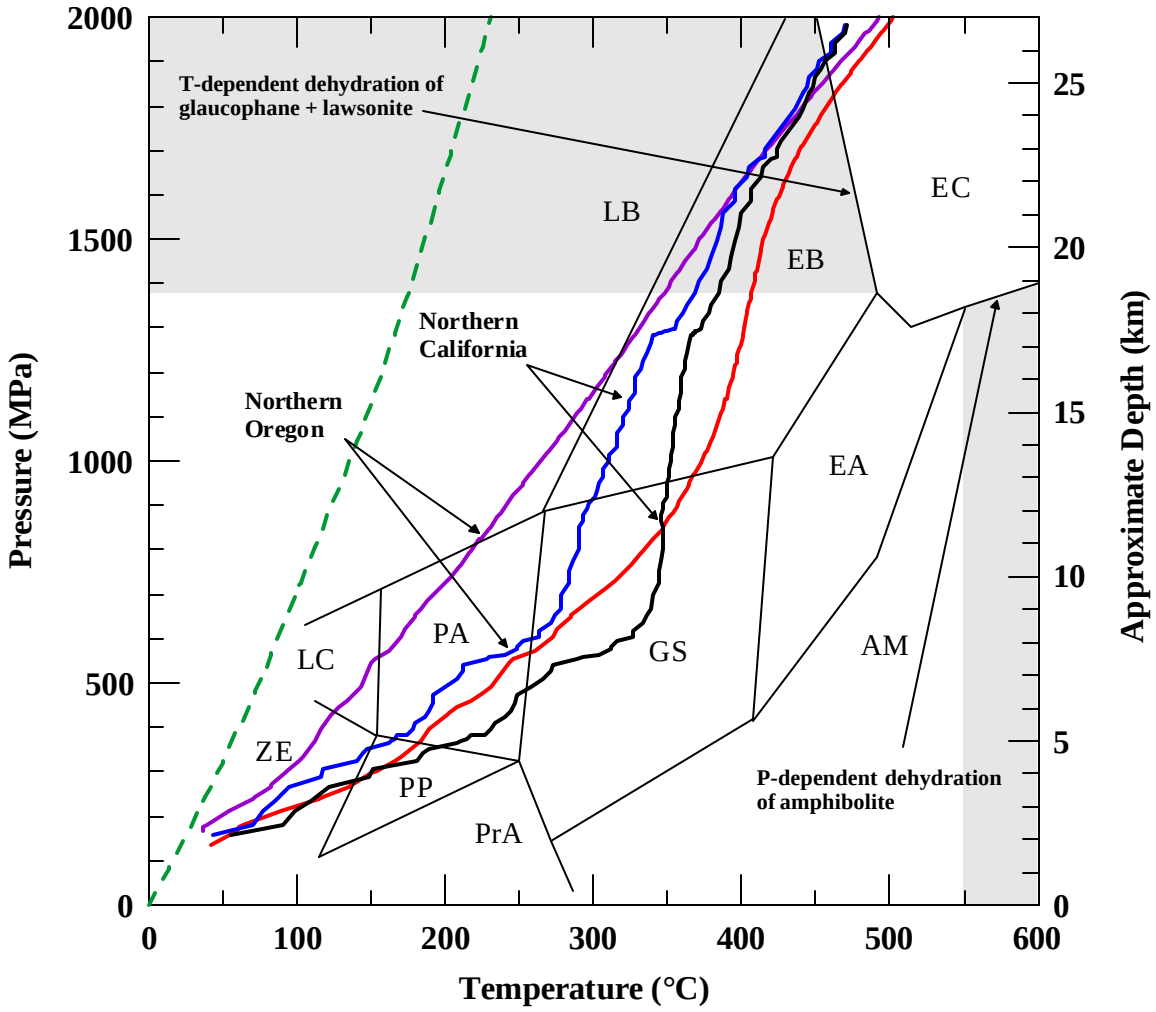
T-dependent dehydration of glaucophane + lawsonite
LB
EC
EB
Northern California
Northern Oregon
EA
PA
LC
GS
AM
ZE
PP
PrA
P-dependent dehydration of amphibolite
Pressure (MPa)
Approximate Depth (km)
Temperature (°C)
2000
1500
1000
500
0
25
20
15
10
5
0
0
100
200
300
400
500
600

Figure 15

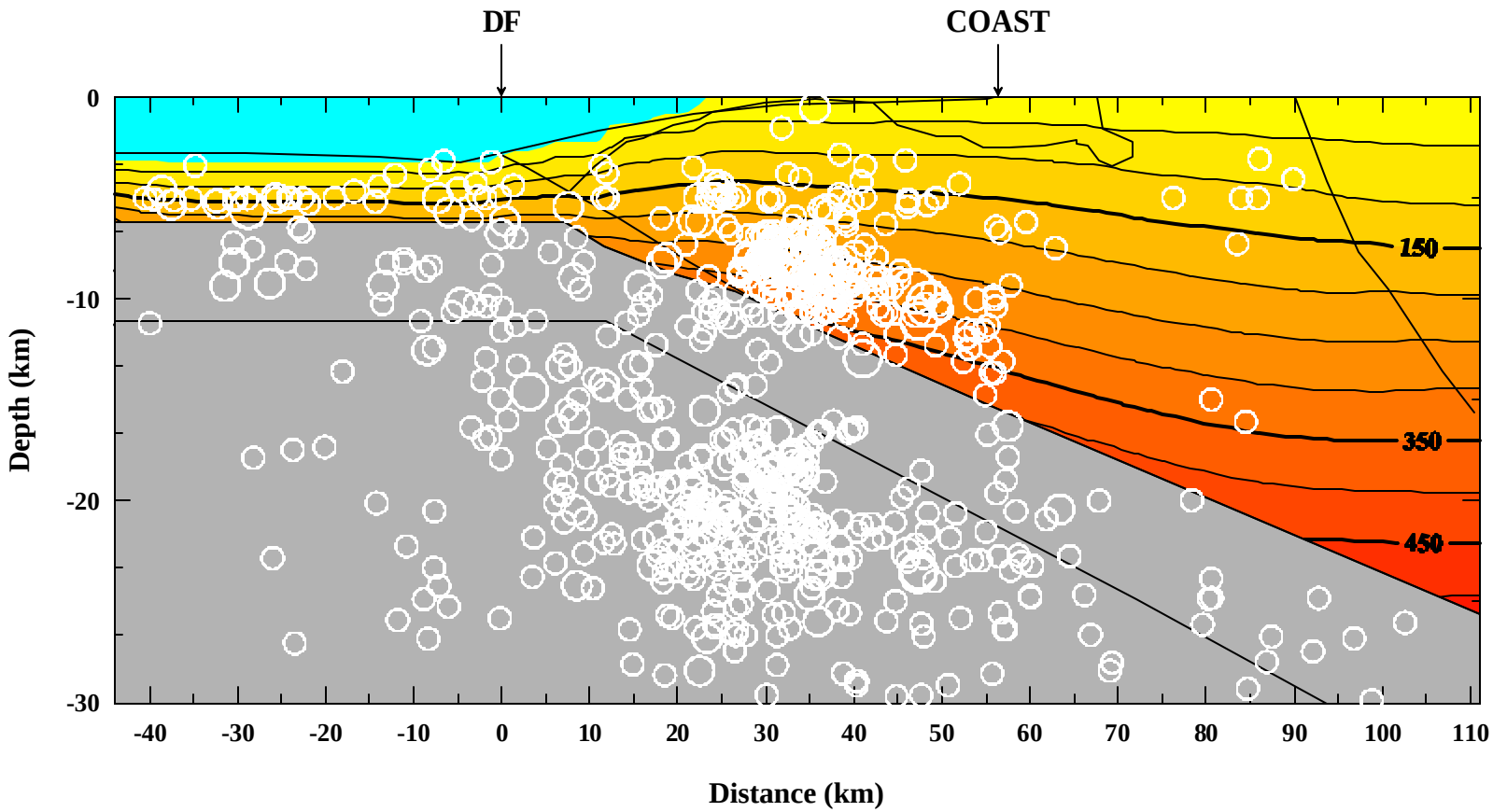
DF
COAST
0
-10
-20
-30
Depth (km)
150
350
450
-40
-30
-20
-10
0
10
20
30
40
50
60
70
80
90
100
110
Distance (km)

Figure A1

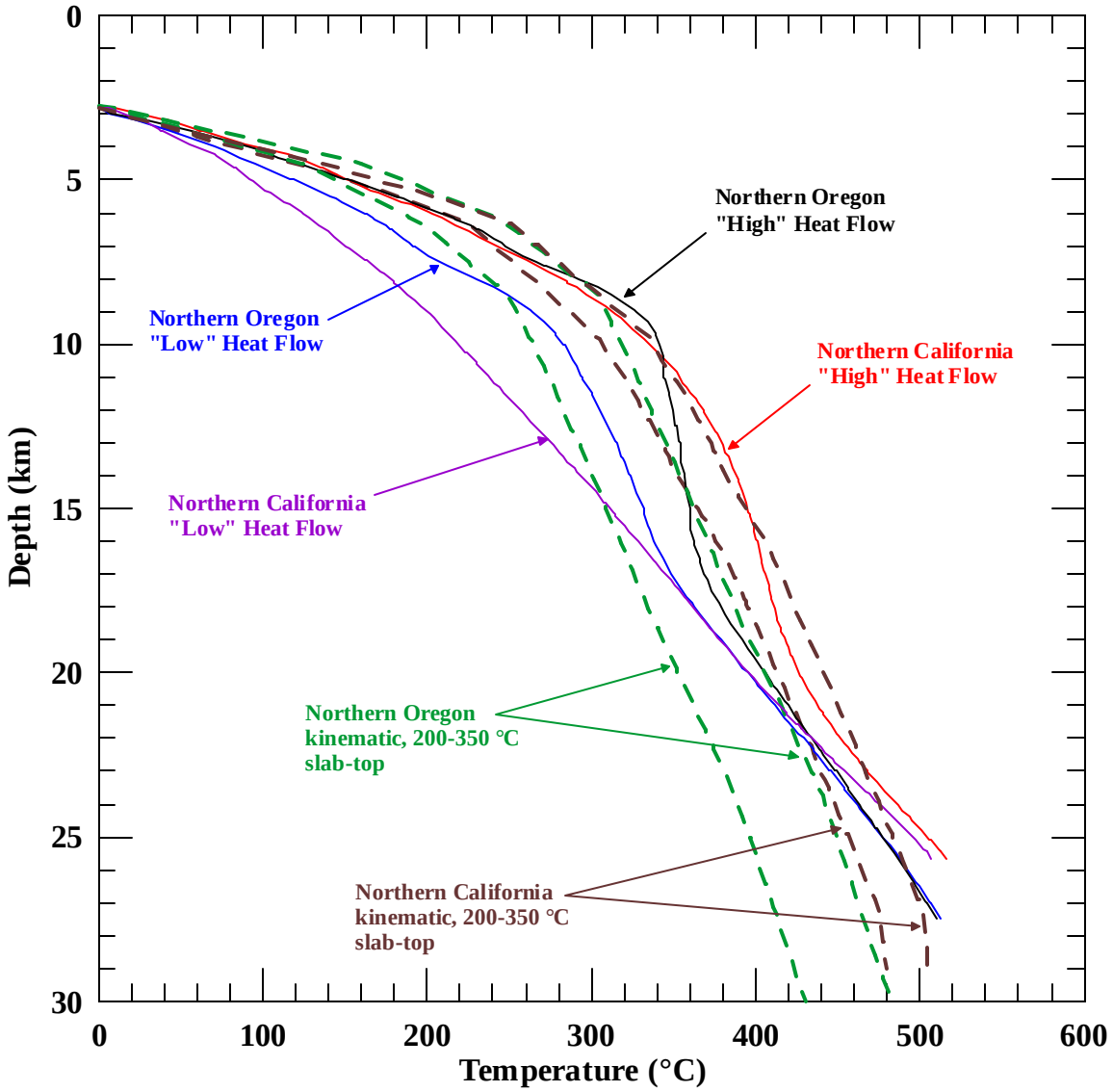
Depth (km)
Temperature (°C)
0
5
10
15
20
25
30
0
100
200
300
400
500
600
Northern Oregon
"High" Heat Flow
Northern Oregon
"Low" Heat Flow
Northern California
"High" Heat Flow
Northern California
"Low" Heat Flow
Northern Oregon
kinematic, 200-350 °C
slab-top
Northern California
kinematic, 200-350 °C
slab-top

Table 1

Cascadia Onshore and Offshore Exploration Wells

Company, Name & Number	Study Name	Lattitude (°N)	Longitude (°W)
Shell Oil Co. P-072 1ET	P-072	46.047	-124.498
Shell Oil Co. P-075 1ET	P-075	46.152	-124.408
Shell Oil Co. P-087 1ET-2ET	P-087	44.222	-124.470
Union Oil Co. Grebe P-093	P-093	44.497	-124.415
Standard Oil Co. Nautilus No. 1 P-0103	P-103	44.858	-124.278
Pan American Oil Co. No. 1, P-0112	P-112	43.263	-124.593
Union Oil Co. Fulmar P-0130	P-130	44.060	-124.647
Linn. Oil Co. Dev No. 1	LCD-1	44.576	-122.843
Humble Oil Co. Wicks No. 1	HWN-1	44.979	-122.646
General Petroleum Corp. Long Bell No. 1	GLB-1	43.802	-123.878
Humble Oil Co. Miller No. 1	HOM-1	44.710	-123.033
Reserve Brewer Oil Co. No. 1	RBN-1	45.008	-123.512
Sinclair Oil & Gas Co. Federal-Mapleton No. 1	SFM-1	44.187	-123.828
Northwest Lumber Co. No. 1	VO-MO-1	47.167	-124.167

Table 2

Calculated Heat Flow in Offshore and Onshore Industry Wells

Well	Depth to, or thickness of (m)		Thermal Resistance (m^2KW^{-1})	Thermal Conductivity ($Wm^{-1}K^{-1}$)		Thermal Gradient (°C/km)		Heat Flow (mWm^{-2})		Heat Generation (μWm^{-3})	
						OFFSHORE					
	Last BHT	No Data	Cumulative	Mean	S.D.	Mean	S.D.	Mean	S.D.	Mean	S.D.
P-075	3092.5	150.0	2032.6	1.45	± 0.14	27.27	± 2.73	39.48	± 5.58	N/A	N/A
P-087	2505.5	150.0	1671.1	1.41	± 0.14	28.34	± 2.83	39.94	± 5.65	0.42	± 0.107
P-093	2904.3	70.0	2156.3	1.31	± 0.13	33.97	± 3.40	44.65	± 6.31	N/A	N/A
P-103	3841.4	150.0	2658.8	1.39	± 0.14	33.25	± 3.33	46.17	± 6.53	N/A	N/A
P-112	1873.3	100.0	1294.4	1.37	± 0.14	31.56	± 3.16	43.23	± 6.11	0.37	± 0.021
P-130	3696.3	150.0	2522.4	1.41	± 0.14	34.72	± 3.47	48.82	± 6.90	0.44	± 0.018
						ONSHORE					
	Last BHT	No Data	Cumulative	Mean	S.D.	Mean	S.D.	Mean	S.D.	Mean	S.D.
GLB-1	2742.0	0.0	1984.5	1.38	± 0.14	26.63	± 2.66	36.8	± 5.20	N/A	N/A
SFM-1	3889.0	0.0	3889.0	1.48	± 0.148	34.96	± 2.369	34.96	± 4.94	N/A	N/A

Table 3

Thermal Modeling Parameters

	K ($Wm^{-1}K^{-1}$)	A (μWm^{-3})
	NORTHERN OREGON	
Oceanic Sediments (0-0.5 km)	0.90	0.43
Sediments (< 5 km)	1.37	0.43
Sediments (> 5 km)	2.00	0.43
Siletz Terrain (< 5 km)	1.37	0.43
Siletz Terrain (> 5 km)	2.25	0.17
Oceanic Crust	2.90	0.00
	NORTHERN CALIFORNIA	
Oceanic Sediments	1.81	0.50
Francisican Complex (<10 km)	2.49	1.10
Francisican Complex (>10 km)	2.20	0.00
Klamath Granite (< 5 km)	2.82	0.45
Klamath Granite (> 5 km)	2.00	0.30
Eel River Sediments	2.00	0.50
Oceanic Crust	2.90	0.00

Table 4

Decollement Integrated Strength

	Thrust Fault		Strike-Slip Fault	
	$P_f = 0$	$P_f = 0.38$	$P_f = 0$	$P_f = 0.38$
		Northern Oregon x 10^{12} Nm^{-1}		
Wet Quartzite	1.3	1.4	1.0	1.1
Diabase	9.8	8.0	9.1	6.7
		Northern California x 10^{12} Nm^{-1}		
Wet Quartzite	0.7	0.6	0.6	0.5
Diabase	4.4	3.8	4.0	3.3
		Southern Mexico x 10^{12} Nm^{-1}		
Wet Quartzite	*16.7*	*12.0*	**	**
Diabase	29.2	30.3	**	**
		Northeastern Japan x 10^{12} Nm^{-1}		
Wet Quartzite	55.9	36.3	**	**
Diabase	*62.0*	*36.6*	**	**